Duong *et al.* (2001) have reported, using a CBF-based fMRI technique, that the size of iso-orientation domains was 0.47 mm. These results suggest that localization of blood flow changes is stronger than that of blood volume changes. In fact, unlike blood volume changes, Duong *et al.*'s experiment did not show any apparent stimulus-nonspecific component of CBF changes. They reported that the average CBF percentage-change ratio of the 'active' to 'inactive' domains was 3.3. This means that the stimulus-specific component of CBF changes was ~70% of the stimulus-nonspecific component. In contrast, this percentage was 2.3% in our measurement of blood volume changes. Further examinations are required to confirm these findings.

Limitation of Analyses of Intrinsic Signals at Multiple Wavelengths

Our analysis of intrinsic signals at multiple wavelengths is based on the assumption that intrinsic signals at visible wavelengths mainly reflect absorption changes of hemoglobin. According to this assumption, we used intrinsic signals at 569 nm as a measure of blood volume changes. We found that the time course of the intrinsic signals at 569 nm was similar to that of the dye-specific absorption changes, which supported the findings of this approach.

Although there was some supporting evidence for intrinsic signals at the isosbestic point of hemoglobin as a measure of blood volume, the isolation of components in intrinsic signals by the recording wavelengths may not be exclusive. For example, components other than hemoglobin absorption changes, such as Ls changes (MacVicar and Hochman, 1991; Kreisman *et al.*, 1995; Holthoff and Witte, 1996; Momose-Sato, 1998; Andrew *et al.*, 1999; Maheswari *et al.*, 2003; Sato *et al.*, 1997; see also Tomita *et al.*, 1983), may be involved in intrinsic signals. One way to better isolate individual components is to use a model that describes light reflection from the cortical surface (Malonek and Grinvald, 1996; Mayhew *et al.*, 1998; Nemoto *et al.*, 1999; Lindauer *et al.*, 2001). We have also analyzed our result using such a model and obtained results consistent with results described above (see Appendix). However, such analyses are not accurate and only provide semi-quantitative results because there is no exact model for changes in reflection from cortical surfaces.

Underlying Mechanisms of Stimulus-specific and Stimulus-nonspecific Components of the Blood Volume Component

In the present study, we have demonstrated that in the cat visual cortex the blood volume changes were resolved in individual iso-orientation domains ~0.6 mm in size. Taking into account the fact that the spatial separation of arteries is larger than that of functional domains, this finding suggests that fine mechanisms of blood volume control exist in fine vessel components, such as precapillary arterioles and capillaries whose spatial separations are definitely <0.6 mm (Pawlik *et al.*, 1981). The presence of such blood volume components is supported by anatomical studies showing contractile structures that may control blood flow and/or volume at the branching points of capillaries (Nakai *et al.*, 1981; Kuschinsky and Paulson, 1992; Shepro and Morel, 1993; Harrison *et al.*, 2002). This stimulus-specific component of blood volume changes, however, is only a small fraction of their stimulus-nonspecific component. To extract stimulus-specific changes in blood volume, for example, subtracting responses evoked by one orientation from those evoked by the orthogonal orientation is necessary in the visual cortex (see also for rodent barrel cortex, Hess *et al.*, 2000). There are three possibilities that explain the origins of stimulus-nonspecific components of the blood volume changes.

First, light scattering can limit the spatial resolution of optical measurement. Orbach and Cohen (1983) demonstrated that the light from a small 40 μm diameter spot spread to ~200 μm in diameter 500 μm away from the spot in cortical tissue. Because of this light scattering, stimulus-specific absorption changes can also spread into cortical domains related to the orthogonal stimulus. Thus, the stimulus-nonspecific component of the signals may be explained by the spread of the stimulus-specific component. If this is the case, however, it is difficult to explain the different ratios of signal magnitudes in the awake state to those in the anesthetized state between stimulus-specific and stimulus-nonspecific components (2.7 versus 3.6 in Fig. 8*C*).

Second, the distinction between stimulus-specific and stimulus-nonspecific components may be related to the specificity of neural activities coupled to the intrinsic signals. Assuming that synaptic activities are coupled to blood volume changes, blood volume changes can be elicited not only at regions where action potentials are generated but also at regions where

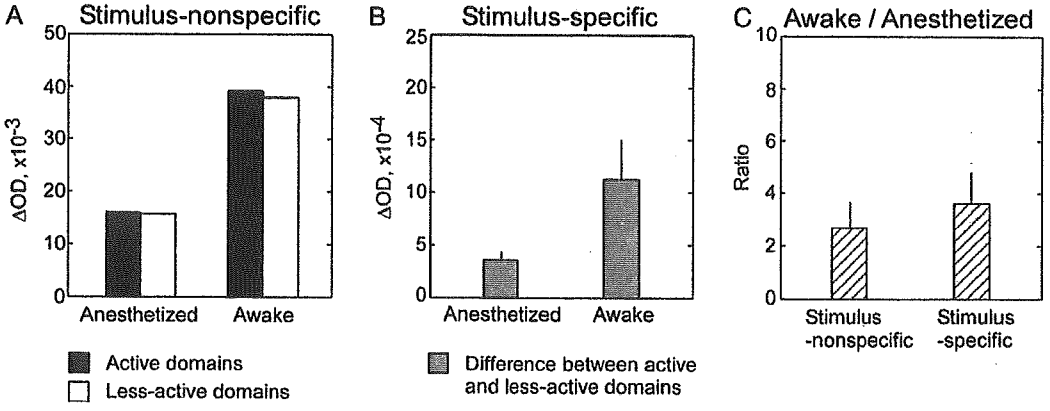

Figure 8. Comparison of signals related to blood volume changes between anesthetized and awake states. (*A*) Stimulus-nonspecific components of the intrinsic signal at 569 nm in active (solid bars) and less-active domains (open bars) for anesthetized (left column) and awake states (right column). The maximum amplitude of the signal in each cat was averaged and plotted ($n = 5$ cats). (*B*) Stimulus-specific components of the intrinsic signal at 569 nm in anesthetized (left column) and awake states (right column). (*C*) Ratios of the signal magnitude in the awake state to that in the anesthetized state for stimulus-nonspecific component (left column) and stimulus-specific component (right column). Error bars indicate one SD of mean obtained from five cats in *B* and *C*.

subthreshold synaptic potentials are generated. The stimulus-nonspecific component may reflect subthreshold synaptic potentials elicited regardless of the stimulus orientation. The mechanisms of coupling between neural activities and intrinsic signals remain issues for future investigations.

Finally, as the most plausible possibility, we consider the contribution of distinct mechanisms of blood flow control in small (precapillary, capillary) and large vessels (artery). Neural activations induce blood flow increases in arteries (Ngai *et al.*, 1988, 1995; Akgoren and Lauritzen, 1999). The arteries do not necessarily govern a particular iso-orientation domain. Blood flow increases in arteries should then induce nonspecific blood volume increases in downstream small vessels (precapillary, capillary and also probably arteriole), though these vessels have a submillimeter spatial precision (but see Iadecola *et al.*, 1997). Assuming supplemental blood flow control mechanisms in a capillary bed, we can expect stimulus-specific and -nonspecific components of blood volume changes. Because this proposal assumes two distinct control mechanisms, we can explain the different ratios of signal amplitudes in awake state to those in anesthetic state between stimulus-specific and stimulus-nonspecific components (Fig. 8*C*). Furthermore, the involvement of different vascular systems in the stimulus-specific and -nonspecific components of blood volume changes also explains the absence of correlation (r = 0.43, P = 0.12, n = 14) between the peak amplitudes of stimulus-specific and -nonspecific components.

Conclusions

In conclusion, we consider that blood volume signals in capillaries include both the stimulus-specific component controlled by the capillaries themselves and the stimulus-nonspecific component elicited by nonspecific blood inflow from upstream arteries. Because of these fine control mechanisms of blood volume, we were able to resolve submillimeter functional structures. The spatial resolution provided by these fine control mechanisms is at least 0.6 mm. This study also suggests that the visualization of blood volume changes can be used for studying brain functions at the submillimeter level.

Notes

We thank Justin Gardner for the development of a stimulus presentation program, and Kazushige Tsunoda for technical assistance throughout the experiments.

Address correspondence to Manabu Tanifuji, Laboratory for Integrative Neural Systems, RIKEN Brain Science Institute, 2-1 Hirosawa, Wakoshi, Saitama, 351-0198, Japan. Email: tanifuji@postman.riken.go.jp.

Appendix

The submillimeter-scale localization of blood volume change was also supported by an additional spectroscopic analysis as described below. We assumed that the change in optical density (ΔOD) was approximately expressed by a linear sum of changes in HbO_2 and Hbr concentrations (Δ[HbO_2] and Δ[Hbr] respectively), and Ls change (ΔLs) as follows:

$$\Delta OD(t)_\lambda = \varepsilon_\lambda^{HbO_2} \cdot d \cdot \Delta[HbO_2(t)] + \varepsilon_\lambda^{Hbr} \cdot d \cdot \Delta[Hbr(t)] - \Delta Ls(t) \qquad (2)$$

where ε_λ is the absorption coefficient at a wavelength, λ (see Fig. 1 legend for the values). The light path length, d, was assumed to be constant at these three wavelengths on the basis of our simulation study (data not shown; see also Shtoyerman *et al.*, 2000). Ls change is also

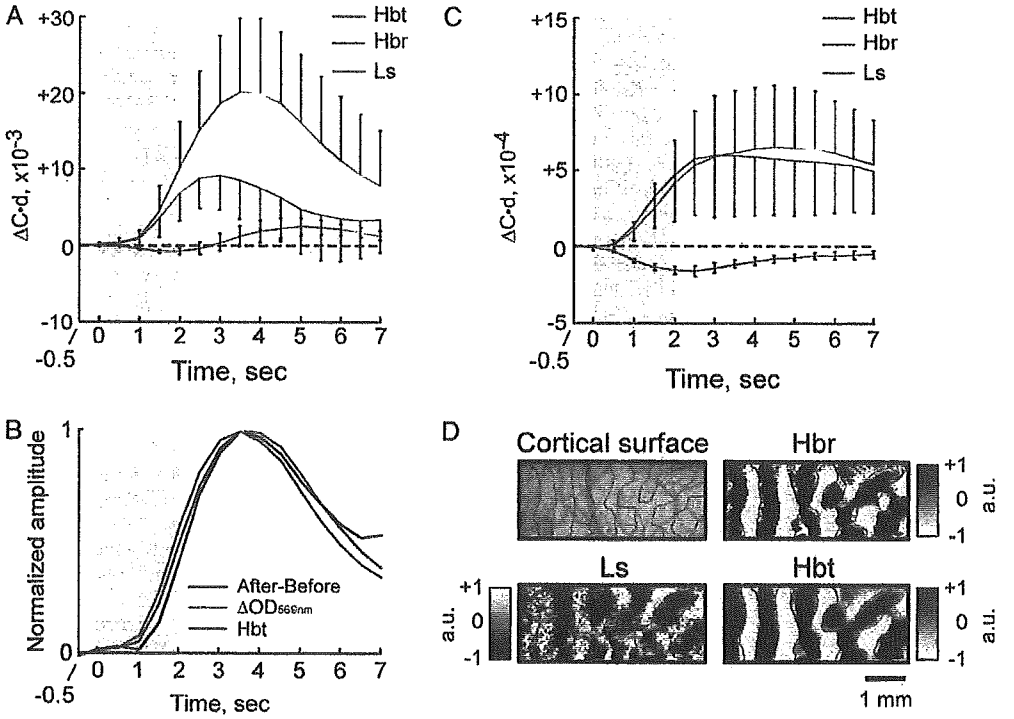

Figure 9. Results of spectroscopic analysis for intrinsic signals. (*A*) Time courses of stimulus-nonspecific components of Hbr, Hbt and Ls, which were calculated from the same data set shown in Figure 3*A*. Error bars indicate one SD of mean obtained from fourteen cats. (*B*) The time course of the Hbt (red line) was plotted together with the time courses of intrinsic signals at 569 nm (green line) and the dye-specific absorption changes (black line). Green and black lines are from the same data shown in Figure 5*B*. Each signal was normalized to its maximum values for comparison. (*C*) Time courses of stimulus-specific components of the Hbr, Hbt and Ls components. (*D*) Differential images obtained from the Hbr, Hbt and Ls. Borders between active and less-active domains at 620 nm (red lines) were superimposed on each panel. This result and the result shown in Figures 2, 4*A* and 6*A* were obtained from the same cortical ROI. Grayscales in Hbr, Hbt and Ls are arbitrary units.

assumed as a wavelength-independent variable on the basis of measurements of Ls changes in brain slices (unpublished observation; see also Cohen and Keynes, 1971; Salzberg *et al.*, 1985; Frostig *et al.*, 1990; Sato *et al.*, 1997; Momose-Sato *et al.*, 1998). The same equation was used in previous studies (Malonek and Grinvald, 1996) and yielded a good approximation for at least Hbr concentration changes in the cat visual cortex (Vanzetta and Grinvald, 1999; Thompson *et al.*, 2003).

To calculate the concentration changes of HbO_2, Hbr and the Ls component from intrinsic signals at 538, 569 and 620 nm, we analytically solved equation (2). The total hemoglobin (Hbt) concentration change was calculated as the sum of HbO_2 and Hbr concentration changes. The calculations were performed for individual stimuli and for control (blank screen) separately. Then, we subtracted the result calculated for the control (blank screen) from those for the stimuli. The product of the light path length, d, and the concentration of each component was used as a measure of each component, because d cannot be determined in the reflection measurement.

Figure 9*A* shows stimulus-induced changes in these three components. The time courses of the Ls component were biphasic, and did not vary greatly among the cats. The time courses of the Hbt concentration changes were monophasic and largely varied among the cats. To confirm whether the Hbt components faithfully represent blood volume changes, we compared the Hbt concentration changes with the stimulus-nonspecific components of the intrinsic signal at 569 nm (green line) and the dye-specific change (black line), and found these three signals showed very similar time courses (Fig. 9*B*). The time courses of the Hbr also varied among the cats. In 4 of 14 cats, the Hbr concentration initially increased after stimulus onset, reached a maximum and decreased below the baseline. However, in most cats, the changes in Hbr concentration did not cross the baseline. Consequently, the average time course of the Hbr concentrations for 14 cats was monophasic. The decrease in the Hbr concentration from the baseline in the late phase was not prominent in our study, but was in the previous studies (Malonek and Grinvald, 1996; Malonek *et al.*, 1997; Nemoto *et al.*, 1997, 1999; Mayhew *et al.*, 1999, 2000, 2001; Shtoyerman *et al.*, 2000, Jones *et al.*, 2001, Lindauer *et al.*, 2001). The discrepancy may be due to the following reasons. First, the solution based on the Beer–Lambert equation is largely affected by light pathlengths that may not be necessarily the same across the recording wavelengths used for the analysis (Mayhew *et al.*, 1999, Lindauer *et al.*, 2001). Second, time courses of intrinsic signals varied (e.g. at 607 nm, data not shown) since the relative contributions of Hbr, Hbt and Ls to the intrinsic signals may not be the same under different experimental conditions, such as individual specificity, anesthetic agents (Lindauer *et al.*, 1993), surgical procedure, recording area, stimulus type and species difference. For example, the time to reach the peak of the intrinsic signals depends on the stimulus frequency and duration (data not shown). Finally, there was no way to evaluate errors associated with the calculation of equation (2), since measurements from three wavelengths are used to obtain three parameters, the concentration changes of HbO_2, Hbr and the Ls component. Thus, in some of our measurements, we might fail to obtain reliable values of Hbr concentration changes, particularly late in the time course.

Similar to the intrinsic signals (Fig. 3*B*), the changes in Hbt and Hbr concentrations in active domains were always larger than those in less-active domains, and Ls changes in active domains were always smaller than those in less-active domains (Fig. 9*C*). To show the spatial pattern of the stimulus-specific components of Hbr, Hbt and Ls, their differential images were averaged from 1 s to 7 s after stimulus onset. As shown in Figure 9*D* the spatial pattern of the stimulus-specific component of the Hbt was almost identical to that of intrinsic signals (red contours) as well as the Hbr and Ls. The correlation coefficients between the differential images at 620 nm and that of Hbr, Hbt and Ls were 0.88, 0.87 and 0.77 ($P < 0.01$), respectively, in this example. We also calculated these correlation coefficients for the other 13 cats, and obtained statistically significant correlations for all of them ($P < 0.01$). The average correlation coefficients for 14 cats with Hbr, Hbt and Ls were 0.52 ± 0.17, 0.63 ± 0.17 and 0.79 ± 0.08, respectively. The highest correlation coefficient in the Ls is probably because of the relatively high contribution of the Ls to intrinsic signals at 620 nm.

References

Akgoren N, Lauritzen M (1999) Functional recruitment of red blood cells to rat brain microcirculation accompanying increased neuronal activity in cerebellar cortex. Neuroreport 10:3257–3263.

Andrew RD, Jarvis CR, Obeidat AS (1999) Potential sources of intrinsic optical signals imaged in live brain slices. Methods 18:185–196, 179.

Bonhoeffer T, Grinvald A (1991) Iso-orientation domains in cat visual cortex are arranged in pinwheel-like patterns. Nature 353: 429–431.

Bonhoeffer T, Grinvald A (1993) The layout of iso-orientation domains in area 18 of cat visual cortex: optical imaging reveals a pinwheel-like organization. J Neurosci 13:4157–4180.

Bonhoeffer T, Grinvald A (1996) Optical imaging based on intrinsic signals: the methodology. In: Brain mapping: the methods (Toga AW, Mazziotta JC, eds), pp. 55–97. San Diego, CA: Academic Press.

Bonhoeffer T, Kim DS, Malonek D, Shoham D, Grinvald A (1995) Optical imaging of the layout of functional domains in area 17 and across the area 17/18 border in cat visual cortex. Eur J Neurosci 7: 1973–1988.

Cannestra AF, Pouratian N, Shomer MH, Toga AW (1998) Refractory periods observed by intrinsic signal and fluorescent dye imaging. J Neurophysiol 80:1522–1532.

Cohen LB, Keynes RD (1971) Changes in light scattering associated with the action potential in crab nerves. J Physiol 212:259–275.

Duong TQ, Kim DS, Ugurbil K, Kim SG (2001) Localized cerebral blood flow response at submillimeter columnar resolution. Proc Natl Acad Sci USA 98:10904–10909.

Frostig RD, Lieke EE, Ts'o DY, Grinvald A (1990) Cortical functional architecture and local coupling between neuronal activity and the microcirculation revealed by *in vivo* high-resolution optical imaging of intrinsic signals. Proc Natl Acad Sci USA 87:6082–6086.

Ghose GM, Ts'o DY (1997) Form processing modules in primate area V4. J Neurophysiol 77:2191–2196.

Grinvald A, Lieke E, Frostig RD, Gilbert CD, Wiesel TN (1986) Functional architecture of cortex revealed by optical imaging of intrinsic signals. Nature 324:361–364.

Harrison RV, Harel N, Panesar J, Mount RJ (2002) Blood capillary distribution correlates with hemodynamic-based functional imaging in cerebral cortex. Cereb Cortex 12:225–233.

Hess A, Stiller D, Kaulisch T, Heil P, Scheich H (2000) New insights into the hemodynamic blood oxygenation level-dependent response through combination of functional magnetic resonance imaging and optical recording in gerbil barrel cortex. J Neurosci 20: 3328–3338.

Holthoff K, Witte OW (1996) Intrinsic optical signals in rat neocortical slices measured with near-infrared dark-field microscopy reveal changes in extracellular space. J Neurosci 16:2740–2749.

Iadecola C, Yang G, Ebner TJ, Chen G (1997) Local and propagated vascular responses evoked by focal synaptic activity in cerebellar cortex. J Neurophysiol 78:651–659.

Jones M, Berwick J, Johnston D, Mayhew J (2001) Concurrent optical imaging spectroscopy and laser-Doppler flowmetry: the relationship between blood flow, oxygenation, and volume in rodent barrel cortex. Neuroimage 13:1002–1015.

Kim DS, Duong TQ, Kim SG (2000) High-resolution mapping of iso-orientation columns by fMRI. Nat Neurosci 3:164–169.

Kreisman NR, LaManna JC, Liao SC, Yeh ER, Alcala JR (1995) Light transmittance as an index of cell volume in hippocampal slices: optical differences of interfaced and submerged positions. Brain Res 693:179–186.

Kuschinsky W, Paulson OB (1992) Capillary circulation in the brain. Cerebrovasc Brain Metab Rev 4:261–286.

Lindauer U, Villringer A, Dirnagl U (1993) Characterization of CBF response to somatosensory stimulation: model and influence of anesthetics. Am J Physiol 264:H1223–1228.

Lindauer U, Royl G, Leithner C, Kuhl M, Gold L, Gethmann J, Kohl-Bareis M, Villringer A, Dirnagl U (2001) No evidence for early decrease in blood oxygenation in rat whisker cortex in response to functional activation. Neuroimage 13:988–1001.

Maheswari RU, Takaoka H, Kadono H, Homma R, Tanifuji M (2003) Novel functional imaging technique from brain surface with optical

coherence tomography enabling visualization of depth resolved functional structure *in vivo*. J Neurosci Methods 124:83–92.
MacVicar BA, Hochman D (1991) Imaging of synaptically evoked intrinsic optical signals in hippocampal slices. J Neurosci 11:1458–1469.
Malonek D, Grinvald A (1996) Interactions between electrical activity and cortical microcirculation revealed by imaging spectroscopy: implications for functional brain mapping. Science 272:551–554.
Malonek D, Tootell RB, Grinvald A (1994) Optical imaging reveals the functional architecture of neurons processing shape and motion in owl monkey area MT. Proc R Soc Lond B Biol Sci 258:109–119.
Malonek D, Dirnagl U, Lindauer U, Yamada K, Kanno I, Grinvald A (1997) Vascular imprints of neuronal activity: relationships between the dynamics of cortical blood flow, oxygenation, and volume changes following sensory stimulation. Proc Natl Acad Sci USA 94:14826–14831.
Mayhew J, Hu D, Zheng Y, Askew S, Hou Y, Berwick J, Coffey PJ, Brown N (1998) An evaluation of linear model analysis techniques for processing images of microcirculation activity. Neuroimage 7:49–71.
Mayhew J, Zheng Y, Hou Y, Vuksanovic B, Berwick J, Askew S, Coffey P (1999) Spectroscopic analysis of changes in remitted illumination: the response to increased neural activity in brain. Neuroimage 10: 304–326.
Mayhew J, Johnston D, Berwick J, Jones M, Coffey P, Zheng Y (2000) Spectroscopic analysis of neural activity in brain: increased oxygen consumption following activation of barrel cortex. Neuroimage 12: 664–675.
Mayhew J, Johnston D, Martindale J, Jones M, Berwick J, Zheng Y (2001) Increased oxygen consumption following activation of brain: theoretical footnotes using spectroscopic data from barrel cortex. Neuroimage 13:975–987.
Momose-Sato Y, Sato K, Hirota A, Kamino K (1998) GABA-induced intrinsic light-scattering changes associated with voltage-sensitive dye signals in embryonic brain stem slices: coupling of depolarization and cell shrinkage. J Neurophysiol 79:2208–2217.
Nakai K, Imai H, Kamei I, Itakura T, Komari N, Kimura H, Nagai T, Maeda T (1981) Microangioarchitecture of rat parietal cortex with special reference to vascular 'sphincters'. Scanning electron microscopic and dark field microscopic study. Stroke 12:653–659.
Narayan SM, Esfahani P, Blood AJ, Sikkens L, Toga AW (1995) Functional increases in cerebral blood volume over somatosensory cortex. J Cereb Blood Flow Metab 15:754–765.
Nemoto M, Nomura Y, Tamura M, Sato C, Houkin K, Abe H (1997) Optical imaging and measuring of local hemoglobin concentration and oxygenation changes during somatosensory stimulation in rat cerebral cortex. Adv Exp Med Biol 428:521–531.
Nemoto M, Nomura Y, Sato C, Tamura M, Houkin K, Koyanagi I, Abe H (1999) Analysis of optical signals evoked by peripheral nerve stimulation in rat somatosensory cortex: dynamic changes in hemoglobin concentration and oxygenation. J Cereb Blood Flow Metab 19:246–259.
Ngai AC, Ko KR, Morii S, Winn HR (1988) Effect of sciatic nerve stimulation on pial arterioles in rats. Am J Physiol 254:H133–139.
Ngai AC, Meno JR, Winn HR (1995) Simultaneous measurements of pial arteriolar diameter and laser-Doppler flow during somatosensory stimulation. J Cereb Blood Flow Metab 15:124–127.
Orbach HS, Cohen LB (1983) Optical monitoring of activity from many areas of the *in vitro* and *in vivo* salamander olfactory bulb: a new method for studying functional organization in the vertebrate central nervous system. J Neurosci 3:2251–2262.
Pawlik G, Rackl A, Bing RJ (1981) Quantitative capillary topography and blood flow in the cerebral cortex of cats: an *in vivo* microscopic study. Brain Res 208:35–58.
Ratzlaff EH, Grinvald A (1991) A tandem-lens epifluorescence macroscope: hundred-fold brightness advantage for wide-field imaging. J Neurosci Methods 36:127–137.
Roe AW, Ts'o DY (1995) Visual topography in primate V2: multiple representation across functional stripes. J Neurosci 15:3689–3715.
Salzberg BM, Obaid AL, Gainer H (1985) Large and rapid changes in light scattering accompany secretion by nerve terminals in the mammalian neurohypophysis. J Gen Physiol 86:395–411.
Sato K, Momose-Sato Y, Arai Y, Hirota A, Kamino K (1997) Optical illustration of glutamate-induced cell swelling coupled with membrane depolarization in embryonic brain stem slices. Neuroreport 8:3559–3563.
Shepro D, Morel NM (1993) Pericyte physiology. FASEB J 7:1031–1038.
Shtoyerman E, Arieli A, Slovin H, Vanzetta I, Grinvald A (2000) Long-term optical imaging and spectroscopy reveal mechanisms underlying the intrinsic signal and stability of cortical maps in V1 of behaving monkeys. J Neurosci 20:8111–8121.
Sibson NR, Dhankhar A, Mason GF, Rothman DL, Behar KL, Shulman RG (1998) Stoichiometric coupling of brain glucose metabolism and glutamatergic neuronal activity. Proc Natl Acad Sci USA 95:316–321.
Silver IA (1978) Cellular microenvironment in relation to local blood flow. Ciba Found Symp:49–67.
Thompson JK, Peterson MR, Freeman RD (2003) Single-neuron activity and tissue oxygenation in the cerebral cortex. Science 299: 1070–1072.
Tomita M, Gotoh F, Yamamoto M, Tanahashi N, Kobari M (1983) Effects of hemolysis, hematocrit, RBC swelling, and flow rate on light scattering by blood in a 0.26 cm ID transparent tube. Biorheology 20:485–494.
Ts'o DY, Frostig RD, Lieke EE, Grinvald A (1990) Functional organization of primate visual cortex revealed by high resolution optical imaging. Science 249:417–420.
Tsunoda K, Yamane Y, Nishizaki M, Tanifuji M (2001) Complex objects are represented in macaque inferotemporal cortex by the combination of feature columns. Nat Neurosci 4:832–838.
Vanzetta I, Grinvald A (1999) Increased cortical oxidative metabolism due to sensory stimulation: implications for functional brain imaging. Science 286:1555–1558.
Villringer A, Them A, Lindauer U, Einhaupl K, Dirnagl U (1994) Capillary perfusion of the rat brain cortex. An *in vivo* confocal microscopy study. Circ Res 75:55–62.
Wang G, Tanaka K, Tanifuji M (1996) Optical imaging of functional organization in the monkey inferotemporal cortex. Science 272: 1665–1668.
Wang G, Tanifuji M, Tanaka K (1998) Functional architecture in monkey inferotemporal cortex revealed by *in vivo* optical imaging. Neurosci Res 32:33–46.

Correlated transition between two activity states of neurons

Go Uchida, Mitsuhiro Fukuda, and Manabu Tanifuji*
Laboratory for Integrative Neural Systems, Brain Science Institute, The Institute of Physical and Chemical Research (RIKEN), Hirosawa 2-1, Wako-shi, Saitama 351-0198, Japan
(Received 18 August 2005; revised manuscript received 15 December 2005; published 14 March 2006)

In order to understand the dynamical properties of a neural network, it is important to characterize the relation between spike trains of two neurons in the network. In this study, we show that in some neuron pairs in inferior temporal cortices of macaque monkeys, spike trains of a pair are described by a two-dimensional Poisson process whose means are modulated by a common two-state Markov process. The common two-state Markov process describes a correlated state transition between firing and nonfiring states of the constituent neurons of the pair.

DOI: 10.1103/PhysRevE.73.031910 PACS number(s): 87.18.−h, 02.50.Ey, 87.17.Nn, 87.10.+e

I. INTRODUCTION

In order to characterize the dynamical properties of a network composed of many neurons, it is important to determine not only the stochastic dynamics of each neuron's spike train but also the relation among the spike activities of neurons in the network. Although the simultaneous recording of spike activities of multiple neurons has progressed rapidly in recent times [1], evaluating the relation among spike activities of more than three neurons is still difficult because statistical methods for analysis of multiple spike trains are limited [2]. However, the relation between spike activities of two neurons in a network can be well characterized by a cross correlogram between spike trains of the neurons. In a previous study, we showed that a broad peak appears in a cross correlogram between spike trains of neurons in inferior temporal (IT) cortices of macaque monkeys [3]. The IT cortex is a visual area that is considered to play an essential role in the perception and recognition of an object. In this study, we formulated a stochastic model for spike trains of a neuron pair in the IT cortex on the basis of cross- and autocorrelation analysis of experimentally recorded spike trains. Using this model, we characterized the relation between the spike activities of an IT neuron pair and the spike train dynamics of the constituent neurons of the pair.

II. EXPERIMENTAL PROCEDURE AND DATA ANALYSIS

We penetrated two to four electrodes (interelectrode distance 580–2380 μm) into the IT cortices of two macaque monkeys and simultaneously recorded spike activities of neurons under anesthetized condition (a mixture of 70% N_2O and 30% O_2, and up to 2% isoflurane). Spontaneous activities of neurons for 1 s were recorded 300–1360 times (trials). The experimental protocol was approved by the Experimental Animal Committee of the RIKEN Institute. All experimental procedures were done in accordance with the guidelines of the RIKEN Institute and the National Institutes of Health.

After the recording, a single cellular spike activity was extracted by applying a template matching method to spike wave forms. Denoting the extracted spike train of a neuron i ($i=1,2$) on the kth trial as $S_i^k(t)$, we estimated average firing rate of the neuron $\hat{R}_i$ as follows:

$$\hat{R}_i = \overline{\hat{H}_i(t)}, \tag{1}$$

where the overbar indicates time average and $\hat{H}_i(t)$ is given by

$$\hat{H}_i(t) = \langle S_i^k(t) \rangle_{tri}. \tag{2}$$

In this equation, $\langle\ \rangle_{tri}$ indicates the trial average. The cross- and autocorrelograms $\hat{R}_{ij}(\tau)$ $(i,j=1,2)$ were also calculated as follows:

$$\hat{R}_{ij}(\tau) = \overline{\langle [S_i^k(t) - \hat{H}_i(t)][S_j^k(t+\tau) - \hat{H}_j(t+\tau)] \rangle_{tri}}. \tag{3}$$

The width of the time bin used in the calculation was 10 ms. The cross correlogram was estimated only for spike trains recorded from different electrodes.

The statistical significance of a peak in the cross correlogram was estimated as follows. First, we shuffled the trial order of the spike trains of one neuron and then calculated the cross correlogram $\hat{R}_{12}^{sh}(\tau)$ as follows:

$$\hat{R}_{12}^{sh}(\tau) = \overline{\langle [S_1^k(t) - \hat{H}_1(t)][S_2^{o(k)}(t+\tau) - \hat{H}_2(t+\tau)] \rangle_{tri}}, \tag{4}$$

where $o(k)$ represents the trial order after the shuffle. This correlogram is called the shuffle correlogram. We shuffled the trial order 1000 times and thereby obtained a total of 1000 shuffle correlograms. On the basis of these shuffle correlograms, we estimated 95% confidence limits of the cross correlograms. If five consecutive bins in the cross correlograms exceeded the upper limit, then we regarded the peak as significant.

III. EXPERIMENTAL RESULTS

We recorded spike activities of neurons from 48 sites in total. The number of single neurons we could extract from a signal recorded at one site was at most 2. We could not

*Electronic address: tanifuji@postman.riken.jp

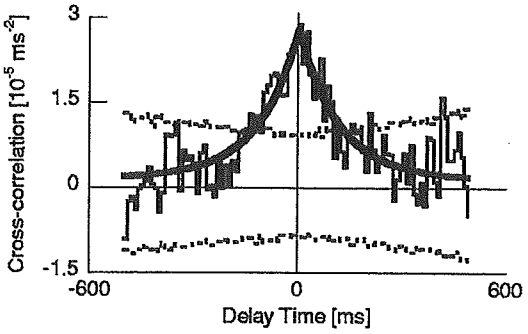

FIG. 1. Cross correlogram of spike trains of an IT neuron pair. Thin solid line for cross correlogram; broken lines for confidence limits of 95%; thick solid line for fitting curve. The fitting function was $y=ae^{-b|\tau|}+c$. $a=2.6\times10^{-5}$ ms^{-2}, $b=8.9\times10^{-3}$ ms^{-1}, $c=1.6\times10^{-6}$ ms^{-2}.

reliably extract spike activities of single neurons from the signals recorded at several sites. As a result, we obtained spike activities of 46 single neurons in total. From these 46 neurons, we obtained 57 neuron pairs. The number of neuron pairs is smaller than that of all possible combinations of the 46 neurons. This is because we did not record spike activities of all 46 neurons simultaneously.

In 17 of the 57 neuron pairs (30%), a significant peak is observed in the cross correlograms. Figure 1 shows an example of a cross correlogram in which a significant peak appears. For this neuron pair, the width of the peak is hundreds of milliseconds. It is probable that this peak resulted from correlation between temporal modulations with a time constant of hundreds of milliseconds involved in the spike trains of the constituent neurons of the pair. This is because there exist components with time constants of hundreds of milliseconds in the autocorrelograms of the constituent neurons [Fig. 2(a)]. Moreover, the components in the autocorrelograms coincide well with the peak in the cross correlogram [Fig. 2(b)]. This result suggests that the temporal modulations involved in the spike trains of the two neurons are perfectly correlated.

To further characterize the temporal modulations in the spike trains, we applied least-squares fitting to the cross correlogram. Then we found that the peak in the cross correlogram is well fitted with an exponential function (Fig. 1). From this result, we can see that the components with a time constant of hundreds of milliseconds in the autocorrelograms are also fitted with the exponential function because these components coincide well with the peak in the cross correlogram (Fig. 2).

There are two well-known stochastic processes whose autocorrelations are an exponential function. One is a two-state Markov process and the other is an Ornstein-Uhlenbeck (OU) process. To examine which process is more appropriate for describing the temporal modulations in spike trains, we formulated stochastic models of spike trains that have temporal modulations described by either the two-state Markov process or the OU process. After the formulation of the models, we estimated all the parameters of each model from experimental data and then we determined which model is more appropriate.

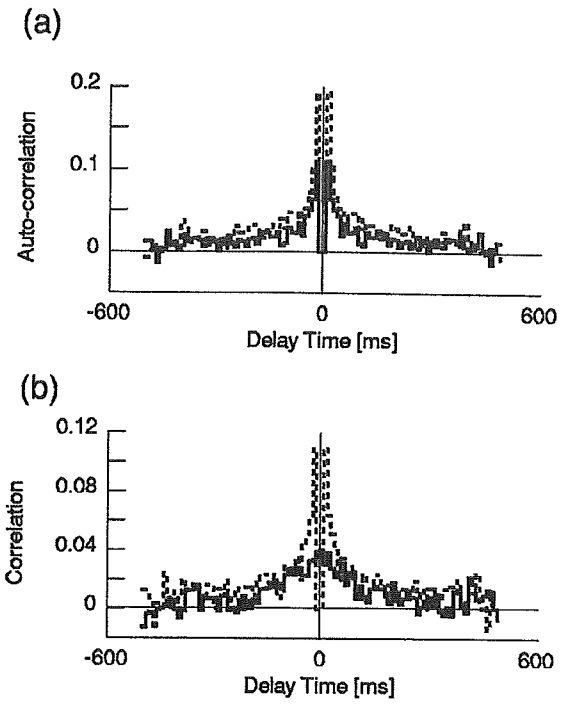

FIG. 2. Autocorrelograms of the neurons (a) and a comparison between the auto- and cross correlograms (b). In (a), solid line for autocorrelogram of one neuron; broken line for that of the other neuron. Each correlogram was normalized by the square of the average firing rate of each neuron. For display, the values at 0 time delay were set to 0. In (b), solid line for the cross correlogram shown in Fig. 1; broken line for the autocorrelogram represented by the solid line in (a). The cross correlogram was normalized by the product of the average firing rates of the neurons.

IV. TWO-DIMENSIONAL POINT PROCESS MODULATED BY A TWO-STATE MARKOV PROCESS

A. Formulation

We first formulated a stochastic model of spike trains of an IT neuron pair that are modulated by a two-state Markov process. In the model, the spike train of each neuron $S_i(t)$ $(i=1,2)$ is denoted by

$$S_i(t) = s_i(t)X(t), \tag{5}$$

where $X(t)$ represents the two-state Markov process common to the two neurons of the pair. In Eq. (5), $s_i(t)$ represents a point process whose average and autocorrelation are given by

$$\langle s_i(t)\rangle = \nu_i, \tag{6}$$

$$\langle [s_i(t)-\nu_i][s_i(t+\tau)-\nu_i]\rangle = f_i(\tau), \tag{7}$$

where $\langle\ \rangle$ represents the sample average, and $f_i(\tau)$ corresponds to a narrower peak that appears in the autocorrelogram at around the 0 time delay of each neuron [Fig. 2(a)] and does not coincide with a peak in the cross correlogram [Fig. 2(b)]. The function $f_i(\tau)$ rapidly approaches 0 as τ increases. We assume that the process $s_i(t)$ is ergodic. In addi-

tion, we assume that $s_1(t)$ and $s_2(t)$ are statistically independent, and $X(t)$ and $s_i(t)$ $(i=1,2)$ are also statistically independent. The state space of $X(t)$ is $X(t)=\{0,1\}$; we call the states $X(t)=1$ and $X(t)=0$ the up and down states, respectively. The transition rate from the down to the up state is denoted by λ, while that from the up to the down state is denoted by μ.

For this model, the average firing rate of each neuron R_i is given by

$$R_i = \nu_i \frac{\lambda}{\lambda+\mu}. \tag{8}$$

The auto- $R_{ii}(\tau)$ $(i=1,2)$ and the cross correlation $R_{12}(\tau)$ functions are given by

$$R_{ii}(\tau) \approx \nu_i^2 \frac{\lambda\mu}{(\lambda+\mu)^2} e^{-(\lambda+\mu)|\tau|} (\tau_s < \tau), \tag{9}$$

$$R_{12}(\tau) = \nu_1\nu_2 \frac{\lambda\mu}{(\lambda+\mu)^2} e^{-(\lambda+\mu)|\tau|}, \tag{10}$$

where τ_s indicates the time constant of the function $f_i(\tau)$. From Eqs. (9) and (10), we can see that after the normalization employed in Fig. 1, the auto- and cross correlations coincide, except at around the zero time delay. Thus, this model is consistent with the result that the auto- and cross correlograms of the pair coincide well except at around the zero time delay (Fig. 2).

B. Parameter estimation

We estimated all the parameters of the model $\{\nu_1, \nu_2, \lambda, \mu\}$ from the experimental data. For the neuron pair used in Figs. 1 and 2, average firing rates of the constituent neurons were estimated from the experimental data using Eq. (1). The estimated average firing rates were 5.560×10^{-3} and 6.087×10^{-3} ms^{-1}. These rates correspond to Eq. (8). Thus, we obtained the following equations:

$$\nu_1 \frac{\lambda}{\lambda+\mu} = 5.560\times10^{-3}\ \text{ms}^{-1}, \tag{11}$$

$$\nu_2 \frac{\lambda}{\lambda+\mu} = 6.087\times10^{-3}\ \text{ms}^{-1}. \tag{12}$$

Furthermore, by comparing the result of the least-squares fitting of the cross correlogram (Fig. 1) and Eq. (10), we obtained the equations

$$\lambda+\mu = 8.9\times10^{-3}\ \text{ms}^{-1}, \tag{13}$$

$$\nu_1\nu_2 \frac{\lambda\mu}{(\lambda+\mu)^2} = 2.6\times10^{-5}\ \text{ms}^{-2}. \tag{14}$$

By solving Eqs. (11)–(14), we obtained $\nu_1=9.9\times10^{-3}$ ms^{-1}, $\nu_2=1.1\times10^{-2}$ ms^{-1}, $\lambda=5.0\times10^{-3}$ ms^{-1}, and $\mu=3.9\times10^{-3}$ ms^{-1}. From these values, we estimated average durations of the up state T_{up} and the down state T_{down} as follows:

$$T_{up} = \frac{1}{\mu} = 2.6\times10^{2}\ \text{ms}, \tag{15}$$

$$T_{down} = \frac{1}{\lambda} = 2.0\times10^{2}\ \text{ms}. \tag{16}$$

In six of the 17 neuron pairs (35%) that have a significant peak in the cross correlograms, we could fit the cross correlograms with exponential functions and estimate the model parameters. The average durations of the up and down states over the six pairs were $4.9\pm1.4\times10^2$ and $3.2\pm1.8\times10^2$ ms, respectively.

C. Evaluation of the model

In order to examine whether our model well describes the experimentally observed spike trains of IT neuron pairs, we estimated the spike count distribution of two neurons from experimentally observed spike trains. We then statistically compared this distribution with that derived from our model using the parameters estimated from the experimental data.

For this purpose, we specified the point process $s_i(t)$ as follows. The time constant of a narrow peak in the autocorrelogram is smaller than that of the two-state Markov process $X(t)$. Thus, as long as we focus analysis on the two-state Markov process, the time constant of the narrow peak can be neglected, i.e., we can approximate the function $f_i(\tau)$ with a Dirac δ function. In addition, the inequality $\nu_i \ll 1$ holds. On the basis of these considerations, we approximated the point process $s_i(t)$ with a Poisson process.

Under this approximation, the spike count distribution of the two neurons during the interval $[0,t]$ is given by the following equation:

$$\begin{aligned} P\{N_1(t)=n, N_2(t)=m\} = P_{nm} \\ = E\left[\frac{\left(\nu_1\int_0^t X(u)du\right)^n}{n!} \exp\left(-\nu_1\int_0^t X(u)du\right) \right. \\ \left. \times \frac{\left(\nu_2\int_0^t X(u)du\right)^m}{m!} \exp\left(-\nu_2\int_0^t X(u)du\right) \right], \end{aligned} \tag{17}$$

where $P\{\cdots\}$ represents the spike count distribution, $N_i(t)$ the spike count of neuron i during the interval $[0,t]$, and $E[\cdots]$ the expectation value. The distribution given by Eq. (17) was calculated from 100 000 sets of two spike trains generated on the basis of the model using the parameters estimated from the experimental data. The calculated distribution was compared with that estimated from experimentally observed spike trains. In the comparison, we calculated a statistic χ^2 given by

$$\chi^2 = \sum_{i=0}^{k}\sum_{j=0}^{l} \frac{(\hat{f}_{ij} - nP_{ij})^2}{nP_{ij}}. \tag{18}$$

In this equation, $\hat{f}_{ij}$ denotes the experimentally observed frequency at spike counts i and j, n the number of trials, and k and l are the maximum spike counts of the two neurons, respectively.

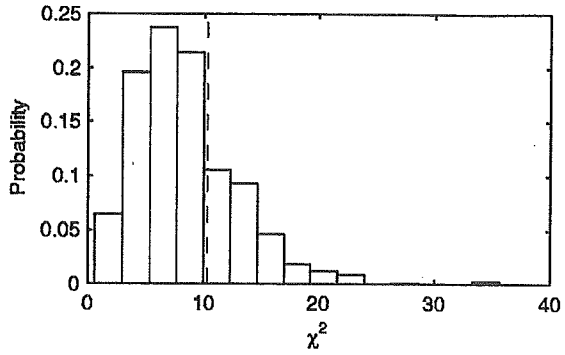

FIG. 3. Probability distribution of χ^2. The dashed line indicates $\chi^2=10.3$.

For a statistical test of χ^2, we require its sample distribution. In order to estimate this distribution, we first generated sets of two spike trains on the basis of our model using the parameters estimated from the experimental data. The spike generation was repeated as many times (trials) as the experiment. The generated spike trains were regarded as experimental data and the spike count distribution that corresponds to the experimentally observed distribution was estimated from the generated spike trains. Subsequently, the parameters of the model were estimated from the generated spike trains in the same manner as in the preceding subsection. On the basis of the model using the estimated parameters, we generated 100 000 sets of two spike trains and calculated the spike count distribution that corresponds to the model distribution. Finally, we calculated χ^2 from the calculated spike count distributions. We repeated this procedure 1000 times. As a result, we obtained 1000 samples of χ^2. On the basis of these samples, we estimated the sample distribution of χ^2 (Fig. 3).

Figure 4 shows the experimentally observed spike count distribution of two neurons whose cross correlogram is shown in Fig. 1 and the distribution based on the model using the parameters estimated from the experimental data. As shown in Fig. 4, the two distributions are very similar. In fact, χ^2 was 10.3, providing $P(\chi^2>10.3)=0.27$ (Fig. 3). Thus, we cannot reject the null hypothesis that the experimentally observed spike count distribution is a sample distribution derived from the model. We obtained the same results for all the six pairs. These results suggest that spike trains of 35% of the IT neuron pairs that have significant correlation are well described by a two-dimensional Poisson process whose means are modulated by a two-state Markov process.

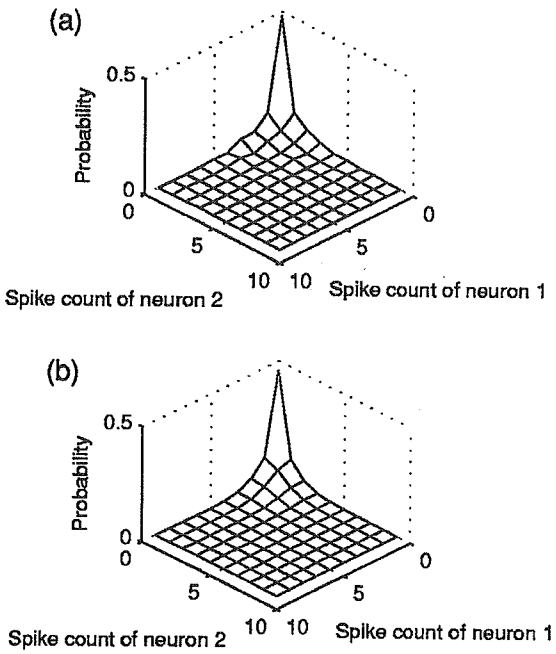

FIG. 4. Spike count distribution of two neurons. Spike counts for 100 ms were estimated. (a) Distribution estimated from the experimental data. (b) Distribution derived from the model using the estimated parameters.

V. TWO-DIMENSIONAL POISSON PROCESS MODULATED BY AN ORNSTEIN-UHLENBECK PROCESS

A. Formulation

Next, we examined whether spike trains of an IT neuron pair can be described by a two-dimensional Poisson process whose means are modulated by an OU process. When the change of firing rates of two neurons is described by an OU process, the firing rate of each neuron, $Y_i(t)$ $(i=1,2)$, is given by

$$Y_i(t) = \sqrt{\alpha_i}\int_{-\infty}^{t} e^{-\kappa(t-s)}dB(s) + \beta_i, \tag{19}$$

$$\langle dB(t)\rangle = 0, \tag{20}$$

$$\langle dB(t)dB(t')\rangle = \delta(t-t')dt\,dt', \tag{21}$$

where α_i, β_i, and κ are constants. From Eqs. (19)–(21), the average firing rate of neuron i is given by

$$R_i = \beta_i. \tag{22}$$

Moreover, the auto- and cross correlations of the spike trains are given by

$$R_{ii}(\tau) = \frac{\alpha_i}{2\kappa}e^{-\kappa|\tau|}(\kappa \neq 0), \tag{23}$$

$$R_{12}(\tau) = \frac{\sqrt{\alpha_1\alpha_2}}{2\kappa}e^{-\kappa|\tau|}. \tag{24}$$

From these equations, we can see that this model can explain the result shown in Fig. 3 when the following equation holds:

$$\frac{\alpha_1}{\beta_1^2} = \frac{\alpha_2}{\beta_2^2}. \tag{25}$$

In addition, to explain the experimental data by this model, the fluctuation of the firing rate must be less than the average firing rate. This is because the firing rate cannot be

negative. Thus, when the variance of the firing rate of each neuron is denoted by V_i, the inequality $V_i \ll R_i^2$ must hold. This inequality can be written as

$$\alpha_i \ll 2\kappa\beta_i^2, \tag{26}$$

because V_i is given by

$$V_i = \frac{\alpha_i}{2\kappa}. \tag{27}$$

B. Parameter estimation and evaluation of the model

From the experimental data, we can estimate all the parameters of the model. The average firing rates of the neurons estimated from the experimental data were 5.560×10^{-3} and 6.087×10^{-3} ms^{-1} (see Sec. IV B). Thus, from Eq. (22) we obtained the equations

$$\beta_1 = 5.560 \times 10^{-3} \text{ ms}^{-1}, \tag{28}$$

$$\beta_2 = 6.087 \times 10^{-3} \text{ ms}^{-1}. \tag{29}$$

In addition, from the result of the least-squares fitting of the cross correlogram (Fig. 1) and Eq. (24), we obtained the following equations:

$$\kappa = 8.9 \times 10^{-3} \text{ ms}^{-1}, \tag{30}$$

$$\frac{\sqrt{\alpha_1\alpha_2}}{2\kappa} = 2.6 \times 10^{-5} \text{ ms}^{-2}. \tag{31}$$

By solving Eqs. (28)–(31) and (25), we obtained $\alpha_1 = 4.2 \times 10^{-7}$ ms^{-3} and $\alpha_2 = 4.6 \times 10^{-7}$ ms^{-3}.

By using the estimated value of α_i and Eqs. (28)–(30), we can estimate the right-hand side of Eq. (26) as follows:

$$2\kappa\beta_1^2 = 5.5 \times 10^{-7} \text{ ms}^{-3}, \tag{32}$$

$$2\kappa\beta_2^2 = 6.6 \times 10^{-7} \text{ ms}^{-3}. \tag{33}$$

From these equations, we can see that the inequality (26) does not hold. We obtained the same results for the six neuron pairs. Thus, this model does not describe spike trains of an IT neuron pair.

VI. DISCUSSION

In this study, we have quantitatively shown that there exist IT neuron pairs whose spike trains are well described by a two-dimensional Poisson process whose means are modulated by a common two-state Markov process. Raster plots of the neurons of a pair confirmed qualitatively that the modulations are not described by an OU process but by a two-state Markov process (Fig. 5). The plots show that in the spike train of each neuron there are two distinct periods: the period during which the neuron fires (firing period) and the period during which the neuron does not fire (nonfiring period). The firing and nonfiring periods are likely to correspond to the up and down states, respectively. The plots also confirmed that a two-state Markov process is common to the neurons of the pair. The firing periods and the nonfiring periods of the neurons overlap well, respectively (Fig. 5).

FIG. 5. Raster plots of the neurons of the pair whose cross correlogram is shown in Fig. 1. The vertical lines indicate spike timing. For each trial, spike timing of one neuron is indicated in the top row and that of the other neuron in the bottom row.

What is the physiological meaning of the states? One of the interpretations is that the two activity states correspond to two states of membrane potential of a neuron [4,5]. For example, the membrane potential of a neuron in the striatum shows two states: the neuron fires during the up state (average potential -49.02 ± 4.16 mV), while it does not fire during the down state (average potential -71.51 ± 3.81 mV) [4]. The relation between the firing and the states of the membrane potential is very similar to our model. In the striatum, the average duration of the up state is 422.57 ± 84.81 ms and that of the down state is 313.01 ± 43.20 ms [4]. These values are comparable to the average durations of the up and down states of IT neurons we estimated. In addition, a correlated state transition of membrane potentials of neurons has been observed in the striatum and other brain areas [6–8]. This is also consistent with the correlated state transition in our model.

The sources of the two activity states and the underlying mechanism to generate a correlated state transition of IT neurons remain unknown. One possible source is the nonlinearity of a single neuron. The dynamics of the membrane potential of a single neuron is described by nonlinear equations. Thus, if an appropriate ion channel exists, the membrane potential can have two stable states [9]. Another possibility is that the two activity states of a neuron emerge only at the network level. For example, an ensemble of neurons in the network composed of excitatory neurons expressing the H current [10] and inhibitory neurons show a correlated transition between two states of membrane potential [11]. In this case, the correlated state transition between two neurons in a network can reflect the state transition of the network.

VII. CONCLUSION

In this study, we have shown that in some of IT neuron pairs, spike trains of a pair are well described by a two-dimensional Poisson process whose means are modulated by a common two-state Markov process that describes a correlated state transition between firing and nonfiring states of the constituent neurons of the pair. This correlated state transition leads to a broad peak in the cross correlogram between

the spike trains of the pair. A broad peak in the cross correlogram has also been observed in the primary visual cortices of macaque monkeys [12] and cats [13]. However, the type of relation between spike activities of neurons that leads to a broad peak remains unknown. Thus, we consider it meaningful to have succeeded in the quantitative characterization of a broad peak in the cross correlogram of an IT neuron pair and revealed the relation between spike activities of the pair.

ACKNOWLEDGMENT

We thank Masato Okada for fruitful discussions.

[1] *Methods for Neural Ensemble Recordings*, edited by M. A. L. Nicolelis (CRC Press, Boca Raton, FL, 1998).
[2] E. N. Brown, R. E. Kass, and P. P. Mitra, Nat. Neurosci. **7**, 456 (2004).
[3] G. Uchida, M. Fukuda, T. Sato, and M. Tanifuji, Abstr. Soc. Neurosci. **28**, 160.13 (2002).
[4] E. A. Stern, A. E. Kincaid, and C. J. Wilson, J. Neurophysiol. **77**, 1697 (1997).
[5] J. Anderson, I. Lampl, I. Reichova, M. Carandini, and D. Ferster, Nat. Neurosci. **3**, 617 (2000).
[6] E. A. Stern, D. Jaeger, and C. J. Wilson, Nature (London) **394**, 475 (1998).
[7] I. Lampl, I. Reichova, and D. Ferster, Neuron **22**, 361 (1999).
[8] R. Cossart, D. Aronov, and R. Yuste, Nature (London) **423**, 283 (2003).
[9] P. Fuentealba, I. Timofeev, M. Bazhenov, T. J. Sejnowski, and M. Steriade, J. Neurophysiol. **93**, 294 (2005).
[10] R. Cossart, D. Aronov, C. Portera-Calliau, and R. Yuste, Abstr. Soc. Neurosci. **28**, 558.3 (2002).
[11] S. Kang, K. Kitano, and T. Fukai, Neural Networks **17**, 307 (2004).
[12] A. Kohn and M. A. Smith, J. Neurosci. **25**, 3661 (2005).
[13] L. G. Nowak, M. H. J. Munk, J. I. Nelson, A. C. James, and J. Bullier, J. Neurophysiol. **74**, 2379 (1995).

ELSEVIER

NeuroImage

www.elsevier.com/locate/ynimg
NeuroImage 30 (2006) 70 – 87

Spatial specificity of the enhanced dip inherently induced by prolonged oxygen consumption in cat visual cortex: Implication for columnar resolution functional MRI

Mitsuhiro Fukuda,[a] Ping Wang,[a] Chan-Hong Moon,[a] Manabu Tanifuji,[b] and Seong-Gi Kim[a,*]

[a]*Brain Imaging Research Center, Department of Neurobiology, University of Pittsburgh, 3025 East Carson Street, Pittsburgh, PA 15203, USA*
[b]*Laboratory for Integrative Neural Systems, Brain Science Institute, The Institute of Physical and Chemical Research (RIKEN), 2-1 Hirosawa, Wako-shi, Saitama 351-0198, Japan*

Received 22 December 2004; revised 13 July 2005; accepted 15 September 2005
Available online 27 October 2005

Since changes in oxygen consumption induced by active neurons are specific to cortical columns, the small and transient "dip" of deoxyhemoglobin signal, which indicates an increase in oxygen consumption, has been of great interest. In this study, we succeeded in enhancing and sustaining the dip in the deoxyhemoglobin-weighted 620-nm intrinsic optical imaging signals from a 10-s orientation-selective stimulation in cat visual cortex by reducing arterial blood pressure with sodium nitroprusside (a vasodilator) to mitigate the contribution of stimulus-induced blood supply. During this condition, intact spiking activity and a significant reduction of stimulus-induced blood volume changes (570-nm intrinsic signals) were confirmed. The deoxyhemoglobin signal from the prolonged dip was highly localized to iso-orientation domains only during the initial ~2 s; the signal specificity weakened over time although the domains were still resolvable after 2 s. The most plausible explanation for this time-dependent spatial specificity is that deoxyhemoglobin induced by oxygen consumption drains from active sites, where spiking activity occurs, to spatially non-specific downstream vessels over time. Our results suggest that the draining effect of pial and intracortical veins in dHb-based imaging techniques, such as blood oxygenation-level dependent (BOLD) functional MRI, is intrinsically unavoidable and reduces its spatial specificity of dHb signal regardless of whether the stimulus-induced blood supply is spatially specific.

Keywords: BOLD; Brain mapping; CBF; CBV; Hemodynamic response; Hypotension; Sodium nitroprusside; Intrinsic signal; Optical imaging; Ocular dominance column; Orientation column

Introduction

Non-invasive mapping of functional cortical columns with common neural properties is critical to understanding how the brain works. Since neural activity induces a focal increase in glucose and oxygen consumption rates, the metabolic response is supposed to be localized to the active site (Lowel et al., 1987; Thompson et al., 2003; Woolsey et al., 1996). Therefore, focal increases of deoxyhemoglobin (dHb) produced by the oxygen consumption change may precisely indicate the location of neural active sites. This expectation was confirmed with intrinsic optical imaging spectroscopy studies (Malonek and Grinvald, 1996), which showed that the early increase of dHb signal (referred to as the "dip", i.e., metabolic response) is better localized to orientation-selective columns in the cat visual cortex than the late decrease of dHb signal due to an over-compensation of cerebral blood flow (CBF). Similarly, cortical columns in the cat visual cortex were successfully mapped only by the early dip in blood oxygenation level-dependent functional magnetic resonance imaging (BOLD fMRI (Ogawa et al., 1990)) but not by late responses at high magnetic fields (Kim et al., 2000a). Thus, the early dip has been of great interest to the functional imaging community (Hennig et al., 1994; Hu et al., 1997; Menon et al., 1995).

However, due to the small and transient nature of the early negative BOLD dip (Buxton, 2001; Duong et al., 2000a; Jezzard et al., 1997; Kim et al., 2000b; Logothetis, 2000) and consequently the low signal-to-noise ratio (SNR), it is difficult to routinely map sub-millimeter-scale functional columns from this dip. Alternatively, brain activity has been commonly mapped from the positive BOLD signal, which indicates a decrease in dHb (i.e., an over-compensated hemodynamic response), although the spatial specificity of this signal is poor compared to metabolic response. The poor spatial specificity of the *late* dHb responses (positive BOLD) can be explained by two hypotheses: (I) widespread CBF and cerebral blood volume (CBV) responses beyond the site of spiking

* Corresponding author. Fax: +1 412 383 6799.
E-mail address: kimsg@pitt.edu (S.-G. Kim).
Available online on ScienceDirect (www.sciencedirect.com).

1053-8119/$ - see front matter © 2005 Elsevier Inc. All rights reserved.
doi:10.1016/j.neuroimage.2005.09.026

activity (Malonek and Grinvald, 1996) and (II) draining of dHb from the active site to non-specific downstream vessels (Duong et al., 2000a). Under normal physiological conditions, the increased oxyhemoglobin supply (i.e., CBF increase) and dHb drain occur simultaneously, making separation non-trivial. In order to decouple these two hypotheses, we propose to modulate the CBF and CBV responses induced by neural activity but without changing neural activity and oxygen consumption rates.

In this paper, the spatial specificity of dHb signals to iso-orientation columns is investigated in the absence of evoked CBF and CBV responses (i.e., conditions matching those of the early dip); these studies were performed in cat visual cortex by using optical imaging of intrinsic signals (OIS), which measures changes in light reflection from the cortical surface (Blasdel and Salama, 1986; Grinvald et al., 1986) accompanied by hemodynamic response to neural activity. To this end, dHb-weighted 620-nm OIS and CBV-weighted 570-nm OIS (for review, see Bonhoeffer and Grinvald, 1996) evoked by orientation-selective gratings were measured at normal and low blood pressure (BP) induced by sodium nitroprusside (sNP). Since blood vessels are considerably dilated at low BP (Endrich et al., 1987; Kontos et al., 1978), any further increase in CBF and CBV due to visual stimulation (i.e., 570-nm OIS) will be significantly reduced. Thus, spatiotemporal dynamics of 620-nm OIS inherently induced by oxygen consumption change can be measured. If, during stimulation at low BP, the 620-nm OIS is not localized to active sites, then the spatial localization of the dHb signal is unlikely due to non-specific blood supply but rather due to the draining of dHb. This investigation will determine the intrinsic spatial specificity of dHb-based functional imaging techniques such as conventional BOLD fMRI and OIS. The companion work studied with fMRI under similar low BP conditions is reported elsewhere (Nagaoka et al., in press).

Materials and methods

Ten cats (1.3–2.0 kg, 11–19 weeks) were used in this study (8 cats for optical imaging and 2 cats for multiple-unit recording). All experimental procedures were approved by the Institutional Animal Care and Use Committee at the University of Pittsburgh.

Animal preparations and physiological conditions

Each cat was initially treated with atropine sulfate (0.05 mg/kg, sub-cutaneous injection) and anesthetized with a sub-cutaneous injection of a mixture of ketamine (20 mg/kg) and xylazine (1 mg/kg). The cat was then intubated and mechanically ventilated (1–2% isoflurane in a mixture of initially 50% N_2O and 50% O_2, and subsequently 70% N_2O and 30% O_2). The femoral artery and vein were cannulated for monitoring arterial blood pressure and injection of drugs, respectively. An intravenous catheter was also inserted into the cephalic vein for continuous infusion of pancuronium bromide (0.2 $mg \cdot kg^{-1} \cdot h^{-1}$) mixed in 5% dextrose Ringer's solution by an infusion pump (Product No. 55-3333, Harvard Apparatus, MA). The cat was then placed in a stereotaxic apparatus (SN-3N, Narishige, Japan). Electroencephalogram (EEG) electrodes were implanted in the frontal bone, and a metal head post and a recording chamber (a 17.5-mm inner diameter) were mounted on the skull with dental acrylic cement. The chamber was placed so that it included A10-P5 and L0-L5 in Horsley–Clarke coordinate; this region roughly corresponds to the location of area 18 in the lower quadrant of the visual field, which is approximately between the vertical meridian and ~25° into the contralateral field, and between the horizontal meridian and ~25° into the lower field (Tusa et al., 1979). After performing a craniotomy inside the chamber, the dura mater was resected. The inside of the chamber was then filled with ~1.5% agarose (Product No. 05065, Fluka BioChemika, Switzerland) and sealed with a round glass cover slip. After surgery, the stereotaxic frame was removed, and the cat was secured by the head post under a macroscope objective for optical imaging. Recordings commenced 1–2 h after the surgery.

To assess the anesthetic level of the cats throughout surgery and experiments, we continuously monitored their rectal temperature, EEG, electrocardiogram, arterial blood pressure, arterial oxygen saturation (SpO_2) and expired-CO_2. These parameters were recorded with BIOPAC (MP150, BIOPAC Systems Inc., CA) for later analyses. Rectal temperature was maintained between 38.1 and 38.7°C with a feedback regulated heating pad system (FHC, Inc., ME). Expired-CO_2 was monitored by capnometer (Capnomac Ultima, Datex Omeda, Finland) and maintained in the range of 3.1–3.9% by adjusting the volume or rate of the ventilator (RSP-1002, Kent Scientific, CT) or both. SpO_2 measured with a pulse oximeter (8600 V, NONIN Medical, Inc., Denmark) was almost 100%. Arterial blood gas analysis (Stat profile pHOx, Nova Biomedical, MA) was performed under normal blood pressure conditions for nine cats (these measurements were not performed for one of the cats used for multiple-unit recording) as follows (mean ± one standard deviation (SD)): P_{CO2} (24.3 ± 1.9 mm Hg, $n = 9$), P_{O2} (204.9 ± 19.1 mm Hg, $n = 8$ (the measurement could not be performed for one of the cats used for optical imaging)), and pH (7.46 ± 0.03, $n = 9$). The isoflurane concentration in a gas mixture of 70% N_2O and 30% O_2 was maintained at the same level during each set of recording for individual cats (usually 0.85–1.0%), which consisted of control (before vasodilator injection), low BP (during injection), and recovery (post-injection) conditions. The range of mean arterial blood pressure (MABP) for control was 76.1–100.9 mm Hg, and that for recovery was 81.6–105.1 mm Hg. These were within the normal range of MABP for cats under ~1% isoflurane anesthesia (Harel et al., 2002a; Zhao et al., 2004a). The range of MABP for low BP was 40.1–55.4 mm Hg.

Sodium nitroprusside-induced low blood pressure

To reduce arterial BP, a vasodilator (sodium nitroprusside dehydrate (sNP), Abbott Laboratories, IL) was injected intravenously for ~25 min (total amount of injection: 0.32–0.59 mg/kg). The sNP (2.5, 5.0 or 7.5 mg) was dissolved in 6 ml of either saline or a mixture of saline and Dextran 40 or 70 (Baxter, IL). The vasodilator infusion rate was dynamically adjusted (between 0.0003 ml/min (initial) and max. 0.08 ml/min to avoid cyanide toxicity) by manually controlling an infusion pump (PHD2000, Harvard Apparatus) to maintain MABP at ~45 mm Hg for ~25 min during optical imaging and for ~15 min during multiple-unit recording. The initial drop in MABP tended to reach ~40 mm Hg, and in two cases, EEG signals became flat at that period. After termination of the vasodilator injection, MABP returned to levels similar to control values (before the vasodilator injection) within ~5 min.

Visual stimuli

All visual stimuli were presented binocularly. Square-wave high-contrast gratings were generated by a graphic video board (VSG2/5, Cambridge Research Systems, United Kingdom) controlled by a custom software written in MATLAB 6.5 (MathWorks, Inc., MA) or Microsoft Visual C++ 6.0 and were presented on a 21-in. CRT monitor (800 × 600 pixels and 100 Hz refresh rate, GDM-F520, Sony). The spatial and temporal frequencies of the gratings were 0.15 cycle (c) per degree and 2 c/second (s) respectively for selective stimulus of area 18 (Bonhoeffer et al., 1995; Issa et al., 2000). The direction of the motion of the gratings was reversed every 0.5 s during visual stimulation. The cat's pupils were dilated with ophthalmic solutions of atropine (1%), phenylephrine hydrochloride (2.5%), and proparacaine hydrochloride (0.5%). Contact lenses (±0.0 D, Danker Laboratories Inc., FL) were fitted to the eyes to prevent corneal drying. The visual field center was roughly estimated by projecting images of optic disks and retinal vessels onto the CRT monitor (Bishop et al., 1962) whose distance was then placed where the best focus of the optic disks and the retinal vessels were obtained (19–31 cm from eyes; visual field 70°–115° wide and 54°–88° high).

Optical imaging

The intrinsic signals were recorded with a custom-made imaging system consisting of tandem lens optics (Ratzlaff and Grinvald, 1991) (i.e., face-to-face combination of a projection lens (50 mm F/1.2, Nikon, Japan) and an objective lens (50 mm F/1.2, Nikon)), a charge-coupled device (CCD) camera (CS8310, 640 × 480 pixels, Tokyo Electric Industry, Japan) and a 10-bit frame grabber board (either Pulsar or Corona-II, Matrox Graphic Inc., Canada). The imaging area was 8.8 × 6.6 mm^2. For seven of the eight cats, the camera was focused on the cortical surface to detect vascular responses on pial vessels. The diaphragm of the projection lens was set to F/2.8 for a large depth of field. For the remaining one cat, the camera was refocused 500 μm below the cortical surface, and the diaphragm of the projection lens was set to F/1.2 for a shallow depth of field as with conventional optical imaging. Since the results obtained from both depth of field were essentially the same, both data were pooled together for analyses. Images were captured at 1/30 s with the frame grabber board controlled by custom software written in Microsoft Visual C++ 6.0. To improve SNR and also reduce data size, temporal averaging of 15 consecutive images and spatial binning of 2 × 2 pixels were performed before saving the acquired images. Thus, the final temporal and spatial resolutions of the saved images were 0.5 s/image and 27.5 × 27.5 μm^2/pixel, respectively. The cortical surface was illuminated through an interference filter (540, 570, or 620 ± 10 nm, Oriel Instruments, CT) using a bifurcated fiber optic bundle (SP77533, Oriel Instruments, CT) that was connected to a tungsten–halogen light source (Model No. 66881 and 68931, Oriel Instruments, CT).

Experimental design

Experimental protocol was outlined in Table 1. In all studies, *cortical surface imaging with 540-nm wavelength* and *four-orientation 620-nm OIS* were performed. Additionally, *single-orientation 620-nm and/or 570-nm OIS* were measured from the same cortical surface, or *multiple neural recordings* were performed as follows.

Cortical surface imaging with 540 nm

Initially, an image of pial vascular pattern was taken with 540-nm wavelength, at which light absorption by hemoglobin is largest.

Four-orientation 620-nm OIS

After acquiring an image of surface vascular patterns, iso-orientation domains for a particular orientation were mapped with 620-nm OIS, which is empirically known to give excellent contrast. To obtain the iso-orientation map efficiently and quickly with the conventional cocktail blank method (described in OIS data analysis), four orientations (0°, 45°, 90°, and 135°) were used with short stimulus duration (2 s) and inter-stimulus interval (2 s). Each stimulation run consisted of 1-s of pre-stimulus homogenous gray (i.e., 2 images) and 2-s stimulus with a moving grating presented at one of the four orientations followed by 1-s of post-stimulus homogenous gray. Twenty runs were repeated for each orientation stimulus (i.e., total recording time, ~2.7 min). The four orientations were presented at a sequential order (from 0° to 45°, 90° and 135°). Based on our experience, the orientation presentation order (e.g., random or sequential presentation) does not affect iso-orientation maps in this short time recording.

Table 1
Experimental design

Experiment	Purpose	MABP	Stimulation	Remarks
Cortical surface imaging with 540 nm	Visualization of vessels	Normal	None	–Separation of tissue and vessel ROIs
Four-orientation 620-nm OIS	Mapping iso-orientation domains	Normal	4 orientations, 2-s stimulation duration 2-s inter-stimulus interval (ISI)	–"Reference" for single-condition iso-orientation maps –Assignment of active and inactive domains for quantitative analyses
Single-orientation 570-nm OIS	Spatiotemporal dynamics of CBV responses	Normal and Low	One orientation, 10-s stimulation 64-s ISI (49 s in one case)	–Determination of whether functional CBV response is decreased at low BP
Single-orientation 620-nm OIS	Spatiotemporal dynamics of dHb responses	Normal and Low	One orientation, 10-s stimulation 64-s ISI	–Enhancement of the dip at low BP –Spatial specificity of the prolonged dip
Multiple-unit recording	Fidelity of neural activity	Normal and Low	4 orientations 10-s stimulation 5-s ISI	–Selectivity of neural activity during low BP

Single-orientation 570- and 620-nm OIS

To determine contribution of CBV response or spatial specificity of dHb signal, 570-nm or 620-nm OIS induced by 10-s visual stimulation were recorded during normal and low BP conditions respectively (n = 5 cats for each wavelength, 2 of them for both wavelengths). The 10-s stimulation duration is relevant to typical block-design fMRI studies. To achieve efficient signal averaging in a limited experimental time during the low BP, only single orientation (0°, 45°, 90°, or 135°) was presented. Twenty single-orientation stimulation runs were continuously acquired at each of normal BP, low BP, and recovery sessions; each run consisted of 10 s of pre-stimulus stationary grating and a 10-s moving grating followed by 54 s (39 s for one 570-nm OIS) of post-stimulus stationary grating to allow the signals to return to pre-stimulus baseline (i.e., inter-stimulus interval was 64 or 49 s). Since results obtained from the two stationary grating periods (64 and 49 s) were essentially the same, both data were pooled together for analyses. For low BP sessions, OIS recordings were started after the MABP reached a desired level (~45 mm Hg). One hour after termination of vasodilator injections, the recovery of the signals was confirmed.

Multiple-unit recording

Spiking activity of multiple neurons was recorded extracellularly from single tungsten microelectrodes (Catalog #UEWLFFL-MNN1E, Frederick Haer and Co. Brunswick, ME) during control (normal BP), low BP, and recovery conditions. The electrode was inserted using a hydraulic microdrive (Narishige MO-81, Japan) into an iso-orientation domain pre-determined with the *Four-orientation 620-nm OIS* recording. The spikes whose amplitudes exceeded a certain threshold, which was set near background activity, were detected at 40 kHz using a spike acquisition system (Plexon Inc, Dallas, Texas). Stimulus consisted of a 2-s homogeneous gray and a 10-s duration moving grating with one of four orientations (0°, 45°, 90°, and 135°) followed by 3-s homogenous gray. For each orientation stimulus, five runs were averaged and spike firing rates in 100-ms bins during stimulation were calculated to determine the selectivity of multiple neurons recorded.

OIS data analysis

All data were analyzed with MATLAB 6.5. After averaging across stimulation runs for each experiment, three sorts of maps (*single-condition raw activity*, *differential iso-orientation, and single-condition iso-orientation* maps) were generated as described in detail below. All the values below are reported as mean ± 1 SD. Statistical significance was examined by ANOVA and two-tailed paired t test. P values of less than 0.05 were considered to be statistically significant.

Averaging across stimulation runs

To increase SNR, OIS runs were averaged. For the experiment of *Four-orientation 620-nm OIS*, all 20 OIS runs (4 s/each run; 1-s pre-stimulus and 3-s post-stimulus onset) were averaged for each orientation. For the experiment of *Single-orientation 570 and 620-nm OIS*, OIS runs were first chopped into a period of 40 s (10-s pre-stimulus and 30-s post-stimulus onset) and screened based on MABP during each 40-s run before averaging. To obtain the MABP during each run, MABP at every cardiac cycle was calculated from the sum of two-thirds of diastolic BP and one-third of systolic BP, and all the MABP for 40 s were averaged. Then one SD of the mean for MABPs across 20 runs (15 runs for low BP sessions, the first five runs were excluded from analyses because the reflected light intensity was not yet stable (see Fig. 2B right panel)) was calculated. Finally, OIS runs whose MABP were within a range of the one SD were averaged. At each BP condition, one averaged run was determined.

Generating single-condition raw activity maps

Then the first frame analysis (for review, see Bonhoeffer and Grinvald, 1996) was performed on the averaged run to reduce the contribution of slow signal fluctuations related with vasomotion (e.g., ~0.1 Hz (Mayhew et al., 1996)) to OIS time courses; the average of two images (i.e., 1 s) just before stimulus onset (pre-stimulus image, R) was subtracted from all images ($R(t)$, t is time from the stimulus onset). The subtraction images ($\Delta R = R(t) - R$) were then divided by the pre-stimulus image (R), so that the pixel values indicate a relative change of reflectance ($\Delta R/R$; 0, no change of light reflection; − (negative sign), decrease of light reflection (i.e., increase of light absorption); + (positive sign), increase of light reflection (i.e., decrease of light absorption)). This first frame analysis was applied to both the *Four-orientation 620-nm OIS* and *Single-orientation 570 and 620-nm OIS* experiments; it is equivalent to a percentage signal change induced by stimulation, which is commonly used in functional MRI. The image generated by the first fame analysis is referred to as a "single-condition raw activity map" (Fig. 1B). All images in the Results section are shown as gray-scale code, where brightness of gray shows intensity of light reflection from pre-stimulus baseline (i.e., darkening and lightening represent decrease and increase in light reflection, respectively).

Generating differential iso-orientation maps

As seen in the single-condition raw activity map (Fig. 1B) or in the map profile (Fig. 1C), OIS is induced not only in the domain specific to a particular orientation but also in all other domains for other orientations, resulting in orientation-specific and -non-specific components (see also Frostig et al., 1990; Grinvald et al., 1986; Malonek and Grinvald, 1996). To remove the orientation-non-specific component and to quantitatively determine iso-orientation domains specific to a particular orientation, we used the cocktail blank data analysis method, which is commonly used to generate iso-orientation maps (for review, see Bonhoeffer and Grinvald, 1996). To this end, first, single-condition raw activity maps for the four orientations (0°, 45°, 90°, and 135°) were obtained from the experiment of *Four-orientation 620-nm OIS* (i.e., 4-s recording for each orientation). Each map was averaged from 0.5 to 3 s after the stimulus onset (the image at 0 s was not included in the average because the signal did not emerge clearly) to increase SNR. Then the resulting four single-condition raw activity maps were averaged to generate a cocktail blank image. Finally, the cocktail blank image was subtracted from the raw activity map with one of the four orientations, and the spatial filter (Fig. 1D) was applied (see below). We will refer to the generated map as a "differential iso-orientation map" (Fig. 1F). This map was used to quantitatively determine iso-orientation domains (see ROI analysis).

Generating single-condition iso-orientation maps

The local modulations specific to a particular orientation (orientation-specific component) can also be extracted from global modulations, which are independent of stimulus orientation

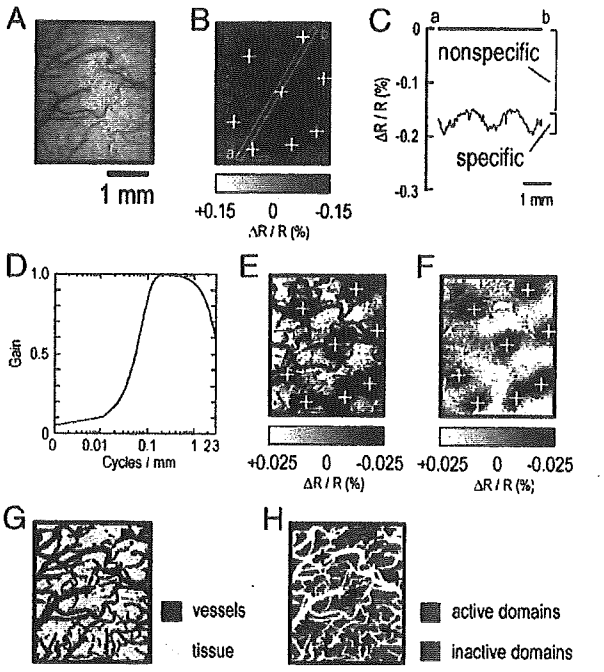

Fig. 1. Cortical activation map generation for analysis of OIS data. (A) A cortical surface image (540 nm) showing vessels for correlation with the maps (620 nm) in panels B, E, F, G, and H. (B) A single-condition raw activity map. The map was obtained by averaging relative change of reflectance images after stimulus onset (0.5–10 s, the image at 0 s was not included in the average because the signal did not emerge clearly). Global absorption increase was observed as a darkening of the entire region (grating at 45° orientation). (C) The profile along the line a-b in map B. (D) Properties of the spatial filter used to remove the global absorption change. (E) A single-condition iso-orientation map. The global absorption change was filtered from the single-condition activity map in panel B. Black patches are now responses specific to the grating at 45° orientation. (F) A differential iso-orientation map. Locations of black patches were determined on this map and marked with white crosses on all maps. (G) Separation of pial vessels (black) and tissue (yellow) based in image A. (H) Separation of active (red) and inactive (blue) domains. Based on the differential iso-orientation map F, the ROI was sub-divided into active and inactive domains for the grating at 45° orientation. Maps were demonstrated with normal BP data (average for 12 runs). See Materials and methods for processing details.

(orientation-non-specific component), by simply applying a spatial filter (Fig. 1D) to the single-condition raw activity map. We will refer to this spatial filtered map as a "single-condition iso-orientation map" (Fig. 1E). The map was obtained from the experiment of *Single-orientation 570- and 620-nm OIS*. This map was used to demonstrate whether iso-orientation domains determined by single-orientation are consistent with those determined by four-orientation stimuli (Figs. 6 and 9). Properties of the filter were determined by the difference of two Gaussian functions ($f(x) = e^{\frac{-x^2}{2\sigma_1^2}} - e^{\frac{-x^2}{2\sigma_2^2}}$, where $\sigma_1 = 0.4$ for low pass frequency, $\sigma_2 = 0.008$ for high pass frequency). The spatial domain image (Fig. 1B) was first transformed into a frequency domain image and then multiplied by the spatial filter (Fig. 1D) to remove low and high frequency components. Finally, the filtered frequency image was inversely transformed into the spatial domain image (Fig. 1E). Black patches in this map represent preferential activation by a particular stimulus orientation.

ROI analysis

To determine spatiotemporal responses induced by a stimulus with a single-orientation, "tissue" and "vessel" regions were chosen (Fig. 1G); the separation between tissue and vessel regions was determined on the cortical surface image taken at 540 nm (see Fig. 1A). Since vessels absorb more light than tissue at this wavelength, vessels appear dark in cortical surface images at 540 nm. Pixels containing signal from pial vessels (a pixel size was $27.5 \times 27.5\ \mu m^2$) were assigned to the vessel region of interest (ROI), and the remaining pixels were the tissue ROI (Fig. 1G). The ratio of vessel ROI to tissue ROI was 0.67 ± 0.06 ($n = 7$ cats). In one cat, due to blurring of pial vessels caused by defocusing camera from cortical surface, the vessel ROI was larger than tissue ROI (the ratio was 1.96), however, this does not affect the result. Tissue ROI was further sub-divided into "active" and "inactive" domains based on the differential iso-orientation map. The pixels having negative values ($-\Delta R/R\%$) in the differential iso-orientation map (Fig. 1F) were assigned to active domains, and the remaining pixels (0% and $+\Delta R/R\%$) were assigned to inactive domains (Fig. 1H). The ratio of active domains to inactive domains was 0.76 ± 0.20 ($n = 8$ cats). Average time courses were plotted from all pixels within each ROI (i.e., vessel, tissue, active, and inactive domains) in the single-condition raw activity maps.

Results

Effects of sNP administration on arterial blood pressure and cortical reflected light intensity

A decrease in arterial blood pressure (BP) causes an increase in CBV to keep CBF rather constant (i.e., autoregulation). Thus, the increase in light absorption (decrease in reflected light) induced by the increase in CBV is expected at low BP. To test this prediction, 570-nm reflected light intensities between normal and low BP were compared. Fig. 2 shows continuous recordings of arterial BP (*A*) and cortical reflected light at 570-nm wavelength (*B*) during normal BP (left panel) and during low BP, induced by sNP injection (right panel). The sNP reduced MABP, systolic and diastolic blood pressure, and also pulse pressure (difference between systolic and diastolic blood pressures) (compare left and right panels of Fig. 2A and insets). Target MABP during sNP injections was at ~45 mm Hg (right panel of Fig. 2A), which may be slightly below the lower limit of CBF autoregulation (Chillon and Baumbach, 2002). Under this condition, vessels are considerably dilated (Kontos et al., 1978), and thus CBV (Schumann-Bard et al., 2005) and total hemoglobin (Ferrari et al., 1992) are increased. In accordance with our expectation, the reflected light intensity gradually decreased from ~800 arbitrary units during normal BP to ~700 units during low BP (Fig. 2B).

To quantitatively compare properties of reflected light between the two BP conditions, *mean* of the reflected light intensity for a 10-s pre-stimulus period was calculated for each of the selected runs (see OIS data analysis in Materials and methods) for both BP conditions. The mean reflected light intensity of 570-nm wavelength during low BP (MABP, 48.3 ± 5.8 mm Hg) for all five cats was 8.0 ± 6.7% less than that during normal BP (MABP, 81.2 ± 5.0 mm Hg). Similarly, the average reflected light intensity at 620 nm during low BP (MABP, 48.1 ± 3.3 mm Hg) for all five cats was reduced by 2.2 ± 1.5%, compared to that with normal BP (MABP, 82.1 ± 3.3 mm Hg). The decreases in reflected light intensity were

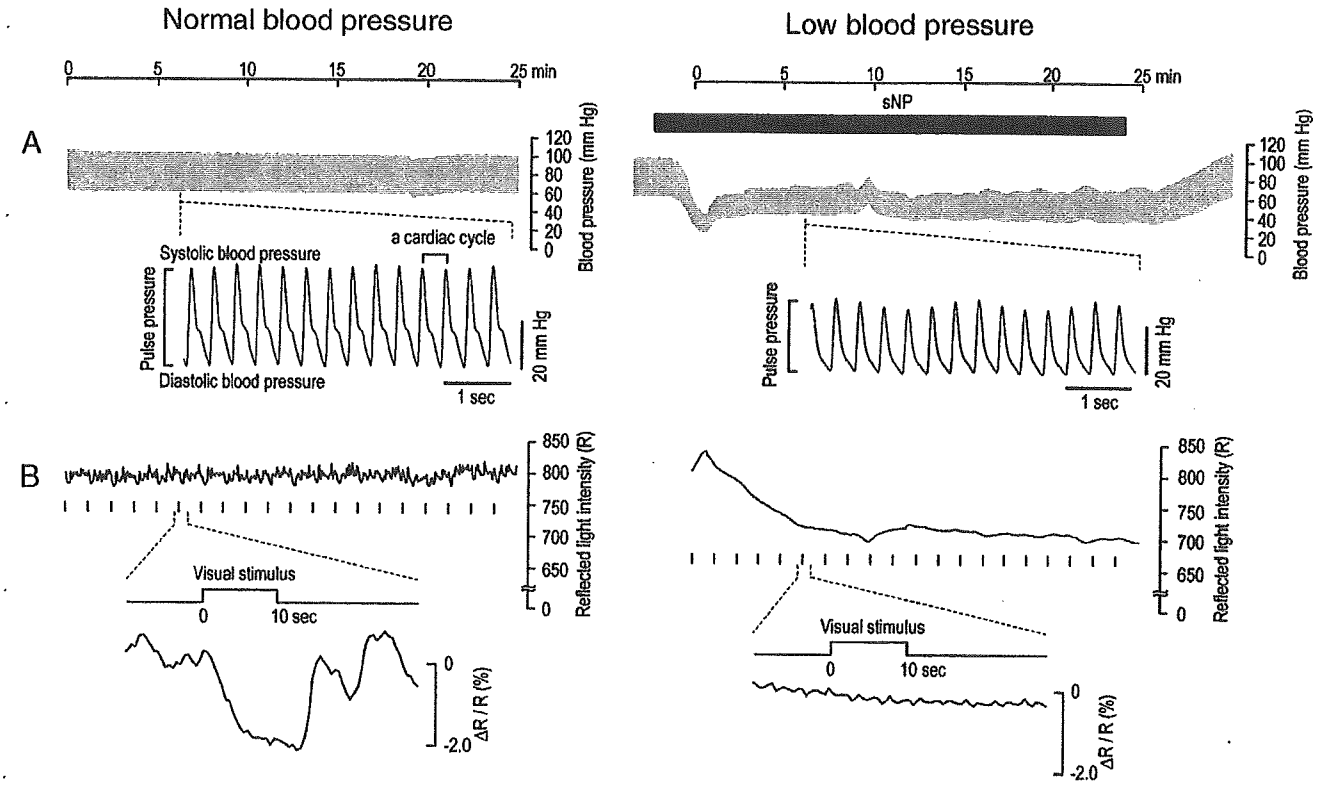

Fig. 2. Effects of sNP administration on BP and cortical reflected light intensity. Continuous recordings of arterial BP and reflected light intensity from the cortex with normal BP (left panels) and those with low BP (right panels) for ~25 min from one study. Time 0 min indicates beginning of OIS recording. (A) Traces of arterial BP. The period of sNP injection is indicated by the horizontal black bar in the right panel. Portions (5 s) of BP traces are expanded to show details in the insets. (B) Traces of reflected light intensity (R) at 570-nm wavelength (obtained from the ROI shown in Figs. 3A and B). The same arbitrary unit is used in both BP conditions. Short vertical bars below the traces indicate the onset of stimulus for each run. Portions (40 s) of reflected light intensity are expanded in insets to show one of the deflections induced by visual stimulation (grating orientation at 45°). Reflected light is shown as a percentage change ($\Delta R/R$). The smaller 0.5 Hz fluctuations are probably due to CBV modulations synchronized with respiration rate.

statistically significant ($P = 0.046$ for 570 nm and 0.029 for 620 nm). This indicates an increase in CBV induced by the decrease of blood pressure.

The reduction of MABP also lessened the fluctuation in the reflected light intensity. As shown in Fig. 2B, the trace of reflected light intensity during normal BP appeared noisy compared to that for low BP. To quantify the fluctuation within a run, one SD of the reflected light intensity for a 10-s pre-stimulus period (SD) was divided by the *mean* of reflected light intensity (SD/mean). The average SD/mean for 570-nm wavelength at low BP (0.14 ± 0.12%, $n = 5$ cats) was significantly smaller ($P = 0.012$) than that at normal BP (0.74 ± 0.40%). Similarly, the average SD/mean for 620-nm wavelength at low BP (0.06 ± 0.02%, $n = 5$ cats) was significantly smaller ($P = 0.002$) than that at normal BP (0.10 ± 0.03%). Since this signal fluctuation is significantly reduced during the low BP condition, smaller stimulation-induced signal changes should be detectable.

Reduction of the stimulus-induced CBV changes during low arterial blood pressure

To evaluate whether the low BP condition can also mitigate the contribution of stimulus-induced CBV changes to OIS, we recorded light reflection changes induced by visual stimulation with 570-nm wavelength (i.e., 570-nm OIS) during both BP conditions. A decrease in light reflection at 570 nm as shown in single-run traces of Fig. 2B inset was observed for every visual stimulus during normal BP (Fig. 2B left), but the signal changes almost disappeared during the low BP condition (Fig. 2B right). This observation was preserved even after averaging all selected runs (Figs. 3A–F, the same cat as Fig. 2). Cortical surface vessels within the ROI are clearly visible during both BP conditions and are dilated for low BP, as can be seen in the pre-stimulus baseline images of Figs. 3A and B. Visual stimulation induced a decrease in light reflection (i.e., a darkening of the cortical images) over the entire ROI as shown in the "single-condition raw activity map" (see OIS data analysis in Materials and methods) of Fig. 3C for normal BP (MABP, 76.1 ± 0.6 mm Hg, average for 17 runs). These global reflection changes almost disappeared in the activity map for low BP (MABP, 45.5 ± 1.8 mm Hg, average for 12 runs) (Fig. 3D). In accordance with the activity maps, the light reflection change induced by stimulation within both tissue and pial vessel regions (see ROI analysis in Materials and methods) was maximum ~2% for normal BP (Fig. 3E) but was maximum ~0.05% for low BP condition in their time courses (note that the vertical scale in Fig. 3F is ten times smaller than that in Fig. 3E). The reduction of signal reached ~90% after 4 s from the stimulus onset (Fig. 3F inset). This signal reduction during low BP was consistently observed across all five cats (Fig. 3G).

To quantitatively compare the magnitude of the 570-nm OIS between normal and low BP conditions, we separately averaged the reflection changes in the regions of tissue and pial vessels

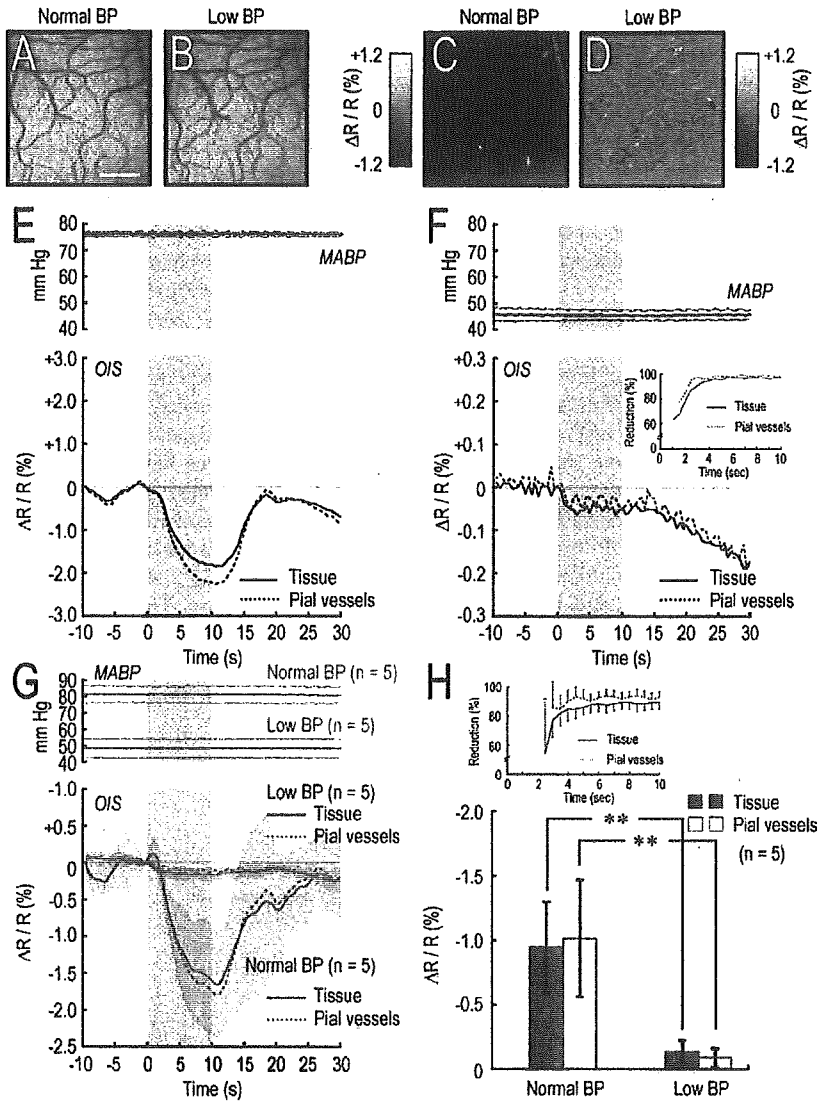

Fig. 3. Reduction of the stimulus-induced CBV changes during low BP. (A–F) Representative data for one cat at 570-nm wavelength. The data are from the same study as Fig. 2. (G and H) Data for all five cats at 570-nm wavelength. (A and B) Images of the cortical surface at baseline during normal (A) and low (B) BP conditions for reference to maps in panels C and D. The scale bar is 1 mm. (C and D) Single-condition raw activity maps for visual stimulation with a grating orientation of 45° during normal (C) and low (D) BP. Data for the maps were averaged from 0.5 to 10 s after stimulus onset. (E and F) (upper panels) Time course of MABP with ±1 SD. (Lower panels) Average time courses for selected runs for one study of 570-nm OIS during normal (E) and low (F) BP from within the regions shown in panels C and D. Solid and dotted lines depict signal originating from tissue and pial vessels, respectively. In the subsequent figures, the 0 time point represents the onset of stimulus and a gray bar indicates the stimulus presentation period. (Inset in panel F) Signal reduction rates over time (solid line, tissue; dotted line, pial vessels). Initial few seconds were not plotted due to low SNR. (G) (upper panel) Average time course of MABP with ±1 SD (n = 5 cats). (lower panel) Average time courses of 570-nm OIS (n = 5 cats) under normal (blue) and low (red) BP. Paler shaded colors indicate ±1 SD. (H) Average magnitudes of the 570-nm OIS (n = 5 cats) from 0 to 10 s after stimulus onset under normal (blue) and low (red) BP conditions. Filled and open bars depict tissue and pial vessels, respectively. Error bars are ±1 SD. The double asterisk (**) indicates $P < 0.01$. (Inset) Average signal reduction rates for five cats over time (solid line, tissue; dotted line, pial vessels). Initial few seconds were not plotted due to low SNR. Error bars are ±1 SD.

during 10-s stimulation (from 0.5 s to 10 s after the stimulus onset, 0 s was not included because the signal did not emerge clearly) for each cat (Fig. 3H). Result with two-way repeated measures ANOVA indicated that the difference between magnitudes of reflection change from tissue vs. pial vessels was not statistically significant ($F_{1,16}$ = 0.007, P = 0.936), while the magnitude difference between normal and low BP was statistically significant ($F_{1,16}$ = 43.604, $P < 6.07 \times 10^{-6}$). The average magnitude of the 570-nm OIS from tissue for all five cats significantly decreased (P = 0.004) during the low BP conditions ($\Delta R/R$, −0.14 ± 0.09%; MABP, 48.3 ± 5.8 mm Hg) compared to that with normal BP ($\Delta R/R$, −0.95 ± 0.35%; MABP, 81.2 ± 5.0 mm Hg), and recovered to a similar magnitude when MABP returned to normal ($\Delta R/R$, −1.33 ± 0.40%; MABP, 88.7 ± 8.0 mm Hg). Thus, the average 570-nm OIS reduction at low BP was 85.8 ± 6.1% (n = 5 cats). A statistically significant reduction of reflection changes was similarly observed in pial vessels ($\Delta R/R$, −1.02 ± 0.45% at normal BP; $\Delta R/R$, −0.09 ± 0.08% at low BP, P = 0.008). As shown in the time

courses of signal reduction rates (Fig. 3H inset), a similar reduction of the signals was mainly observed in later time points (4–10 s from the stimulus onset). These results are consistent with our expectation that the 570-nm OIS would be considerably reduced by decreasing the BP. This suggests that the 570-nm OIS is predominantly derived from changes in total hemoglobin content (i.e., CBV) as has generally been assumed (for review, see Bonhoeffer and Grinvald, 1996), and thus stimulus-induced CBV changes were greatly reduced under low BP conditions.

Preservation of neural activity during low arterial blood pressure

The reduction of stimulus-induced CBV during low BP is due to a loss of vasodilation capacity or a decrease of neural activity. To test whether a decrease in neural activity is the major source of reduced evoked CBV responses, multiple-spiking activities of neurons were recorded in two cats. Fig. 4A shows examples of spike firing rates of multiple neurons for a 10-s visual stimulation periods during normal (left panel) and low BP (right panel) conditions. Although spiking activity from multiple neurons transiently disappeared for the initial few minutes after the MABP reduction, the activity recovered to the pre-infusion levels. The initial loss of neural activity may be related to hypotension ischemia (Sato et al., 1984) rather than direct sNP effects (see Discussion); an initial drop of MABP to ~40 mm Hg may extremely slow down or stop local blood perfusion at that period. This would cause a decrease in oxygen tension in tissue, leading to a decrease of cerebral metabolic rate of oxygen consumption ($CMRO_2$). Spiking activity only disappeared during initial MABP of ~40 mm Hg period and recovered when MABP returned to ~45 mm Hg (Fig. 4A). If sNP itself affected spiking activity, the activity would not be recovered during sNP administration. This initial deactivation (~5 min) may also be related with the initial unstable light reflectance (see Fig. 2C).

To quantitatively compare the magnitude and selectivity of neural activity between normal BP (control) and low BP conditions, the average spike frequency during 10-s stimulation for 5 runs was calculated for each orientation (0°, 45°, 90°, and 135°) for both BP conditions. As shown in Fig. 4B, orientation tuning at low BP (red lines) was essentially the same as that in normal BP (blue lines). Furthermore, average dynamics of the spike firing rates at preferred and anti-preferred (i.e., orthogonal to the preferred) orientation was similar between two BP conditions (Fig. 4C, MABP, 95.7 ± 9.0 mm Hg (normal) vs. 47.5 ± 3.2 mm Hg (low), $n = 4$ sites). These data show that neural activity does not change between normal and low BP conditions, and therefore, the significant reduction of 570-nm OIS we observed during low BP conditions is not due to a decrease of neural spiking activity.

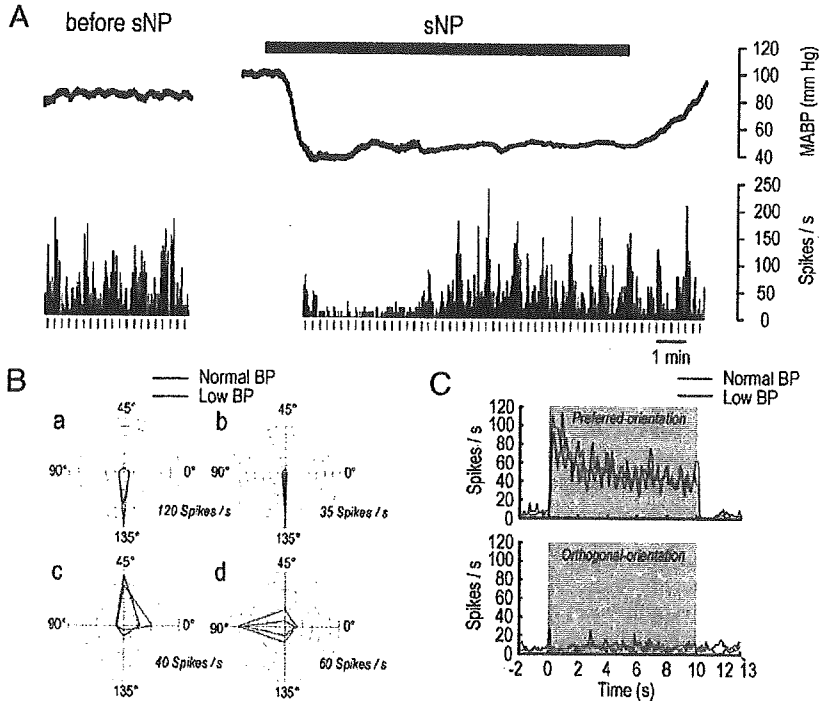

Fig. 4. Preservation of neural activity during low BP. (A) Example of spike activity of multiple neurons induced by a 10-s visual stimulation during normal (left panels) and low BP (right panels); MABP (upper), spike firing rates in 100-ms bins (lower). The period of sNP injection is indicated by the horizontal black bar in the right upper panel. Vertical ticks below the lower traces represent stimulus onset for each run. Runs recorded at the preferred orientation are indicated by red ticks. (B) Orientation tuning curves of all recorded neurons ($n = 2$ cats). Blue and red lines represent the average for 5 runs at normal and low BP, respectively. MABP at each run was determined by averaging the values for 15 s (from 2 s pre-stimulus to 13 s after stimulus onset), yielding normal/low MABP (mm Hg) average values for 5 runs of (a) 100.9 ± 2.1/52.2 ± 2.2, (b) 98.7 ± 1.8/44.9 ± 2.9, (c) 82.3 ± 1.2/46.6 ± 2.1, (d) 100.7 ± 1.8/46.8 ± 2.1. Iso-contours indicate the same firing rates (spikes/s). The center is 0 spike/s. The inner iso-contour firing rate can be obtained by dividing the given firing rate by the number of contours. Neurons a and b were recorded from the same penetration track in one cat (500 μm and 300 μm below the cortical surface, respectively). Neurons c and d were recorded at two different penetration sites from another cat (both recorded at 300 μm). Activity shown in panel A is neuron c. (C) Peri-stimulus time histograms in 100-ms bins during normal (blue) and low (red) BP conditions with 10-s visual stimulation, where spike firing rates at preferred (upper panel) and orthogonal (lower panel) orientations for neurons at 4 different sites (a–d in panel B) were averaged.

Enhancement of the dip during low arterial blood pressure

The reduction of CBF and CBV at low BP without a concomitant decrease of neural activity will cause dHb increase to be sustained during stimulation. Thus, the dip in the dHb-weighted 620-nm OIS at low BP is expected to continue during the entire 10-s stimulation period, unlike the 620-nm OIS at normal BP.

Typical spatiotemporal responses of the 620-nm OIS for 10-s stimulation at normal and low BP from one cat are shown as single-condition raw activity maps in Figs. 5A and B, respectively, and as the average time courses from tissue and pial vessels in Fig. 5C. During the normal BP condition (MABP, 81.5 ± 3.8 mm Hg, average for 12 runs), decreases of light reflection induced by visual stimulation were highly localized to patches within ~2 s after the stimulus onset (see 1.5 s in Fig. 5A) which is consistent with the previous reports (Grinvald et al., 2000; Malonek and Grinvald, 1996). Afterwards, they quickly spread throughout the cortex (see darkening of the cortical image in the panel of 5.0 s), followed (at normal BP) by a global increase of light reflection (see lightening of the cortex in the panel of 10.0 s). The biphasic time course of the 620-nm OIS at normal BP (blue lines in Fig. 5C) suggests that dHb contents initially increase due to increases in oxygen consumption by active neurons (Vanzetta and Grinvald, 1999; but see Lindauer et al., 2001), then later decrease due to over-compensation of CBF (Fox and Raichle, 1986). Both tissue and pial vessels behaved similarly at normal BP over the entire time course, and results were consistent in all 5 cats (Fig. 5D). During the low BP conditions (MABP: 51.4 ± 1.4 mm Hg, average for 11 runs), light reflection decreased at 1.5 and 5.0 s (Fig. 5B), similar to normal BP conditions, but a continuing decrease in light reflection (i.e., a prolonged dip) was observed over the cortical region during the entire stimulation period (see 10.0 s in Fig. 5B). The monophasic time courses were observed similarly in both tissue and pial vessels (red lines in Fig. 5C). This was consistent across all five cats (Fig. 5D). The result suggests that a prolonged increase in dHb content is detectable at low BP because the sustained increase in oxygen metabolism is not compensated by further increases in oxygen supply due to CBF and CBV changes (Offenhauser et al., 2005).

To quantitatively compare the dHb signals between normal and low BP conditions, the maximum magnitude of the dip during the 10-s stimulation was determined (time for maximum tissue signal was chosen for both tissue and pial vessels). Result with two-way repeated measures ANOVA indicated that the difference between magnitudes of reflection changes from tissue vs. pial vessels was

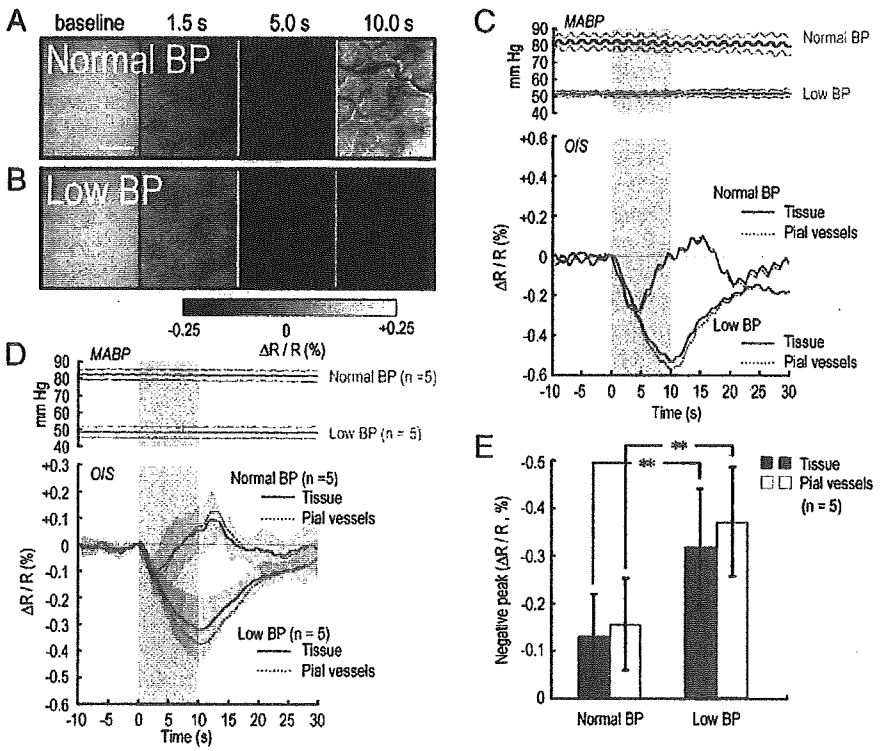

Fig. 5. Enhancement of the dip during low BP. (A–C) Representative data for one cat at 620-nm wavelength. The data are from the same study as Fig. 1. (D and E) Data for all five cats at 620-nm wavelength. (A and B) Images of the cortical surface at baseline (left panels) and single-condition raw activity maps for visual stimulation with a grating orientation of 45° at 1.5, 5.0, and 10 s after stimulus onset during normal (A) and low (B) BP. The cortical surface images were sharpened by Photoshop (Adobe) to enhance vascular patterns. Note that vessels were dilated at low BP. The scale bar is 1 mm. (C) (upper panel) Time courses of MABP with ±1 SD (n = 5 cats). (lower panel) Time courses of the 620-nm OIS from the region shown in panels A and B. Reflection changes from tissue (solid lines) and pial vessels (dotted lines) are plotted for both normal (blue) and low (red) BP. (D) (upper panel) Average time courses of MABP with ±1 SD. (lower panel) Average time courses of the 620-nm OIS (n = 5 cats) with normal (blue lines) and low (red) BP. Solid and dotted lines depict signal from tissue and pial vessels, respectively. Paler shaded colors indicate ±1 SD. (E) Average magnitudes of the minimum 620-nm OIS (n = 5 cats) for normal (blue) and low (red) BP conditions where maximum negative deflections of tissue signal during the 10-s stimulation in individual cats were averaged. Filled and open bars depict signal from tissue and pial vessels, respectively. For calculations, the same time point was chosen for pial vessel signal as for the tissue signal. Error bars are ±1 SD. The double asterisk (**) indicates $P < 0.01$.

not statistically significant ($F_{1,16}$ = 0.646, P = 0.433), while the magnitude difference between normal and low BP was statistically significant ($F_{1,16}$ = 17.499, P = 0.001) (Fig. 5E). In both tissue and pial vessels, the average maximum dip for all five cats with low BP ($\Delta R/R$: −0.32 ± 0.12% for tissue, −0.37 ± 0.12% for vessels, MABP: 48.1 ± 3.3 mm Hg) was significantly larger (P = 0.002 for tissue, P = 0.0008 for vessels) than that with normal BP (MABP, 82.1 ± 3.3 mm Hg; $\Delta R/R$, −0.13 ± 0.09% for tissue; −0.16 ± 0.10% for vessels). The responses recovered when MABP returned to normal (MABP, 84.0 ± 2.0 mm Hg; $\Delta R/R$, −0.13 ± 0.03% for tissue; −0.16 ± 0.04% for vessels). Similar magnitudes of reflection changes in pial vessel and tissue ROIs suggest that increased dHb in tissue drains to the pial vessels.

Preservation of orientation selectivity of deoxyhemoglobin signals during low arterial blood pressure

Since neural spiking activity was preserved during the low BP condition (see Fig. 4), orientation selectivity of oxygen consumption in *neurons* is also expected to be the same as it is for normal BP. To test this prediction, we examined selectivity of the 620-nm OIS for normal and low BP because the 620-nm OIS originates mostly from dHb content changes in *blood*, which can be related to the oxygen consumption by *neurons*. For this purpose, "single-condition iso-orientation maps" (see OIS data analysis in Materials and methods) were calculated to obtain spatial patterns of the 620-nm OIS specific to a stimulus orientation (Grinvald et al., 1986; Shmuel and Grinvald, 1996); the orientation-non-specific signal is removed from this map. It should be noted that the non-specific signal is usually 5–10 times larger than the orientation-specific signal (e.g., the gray scale range of Figs. 5A and B was five times larger than that of Figs. 6A and B). In a representative study, the spatial pattern of iso-orientation domains (black patches marked with white crosses) with normal BP (Fig. 6A) appears essentially the same as that for low BP (Fig. 6B). The correlation coefficient between two single-condition maps for a corresponding 100 × 100-pixel (2.75 × 2.75 mm^2, white rectangles in Figs. 6A–D) region (not including pial vessels, the cortical vasculature is shown in Fig. 6C) was significantly high (R = 0.62, P < 0.01; for 5 cats R = 0.51 ± 0.07). The location of iso-orientation domains was confirmed by a "differential iso-orientation map" at normal BP (see OIS data analysis in Materials and methods) shown in the Fig. 6D. Negative percentage values (i.e., black patches) in the differential iso-orientation map are referred to as "active domains" and remaining area as "inactive domains" (see also OIS data analysis in Materials and methods).

To determine whether orientation selectivity in 620-nm OIS is preserved at low BP, single-condition iso-orientation maps for one stimulus orientation at both low BP and at normal BP (as a control) obtained from the experiment of *Single-orientation 570 and 620-nm OIS* were compared with differential iso-orientation maps for four stimulus orientations obtained from the experiment of *Four-orientation 620-nm* (for each experiment, see Materials and methods and Table 1) (Fig. 6E). The correlation coefficient was calculated between the single-condition iso-orientation maps and the differential iso-orientation maps for corresponding 100 × 100-pixel regions. For the *low* BP single-condition iso-orientation data, the highest positive correlation was observed when the grating orientation was the same as the differential iso-orientation map (i.e., angular difference, 0°), while the highest negative correlation was detected when orientations were orthogonal (i.e., angular difference, 90°). The difference between normal vs. low BP was not statistically significant (two-way repeated measures ANOVA, $F_{1,4}$ = 2.364, P = 0.199), suggesting that dHb signals at both normal and low BP show similar orientation selectivity.

Furthermore, we calculated the magnitude difference of the OIS between active and inactive domains, which likely correlate with spike firing rates of neurons in the active domain (Shmuel and Grinvald, 1996). To calculate the magnitude difference in OIS, time courses of the 620-nm OIS in active and inactive domains were separately obtained. Then the signals during 10-s stimulation (from 0.5 to 10 s after the stimulus onset, 0 s was not included because the signal did not emerge clearly) were averaged. The mean magnitude difference between active and inactive domains for the 620 nm OIS (n = 5 cats) at normal BP (0.03 ± 0.01%) was statistically not different (P = 0.25) from that with low BP (0.04 ±

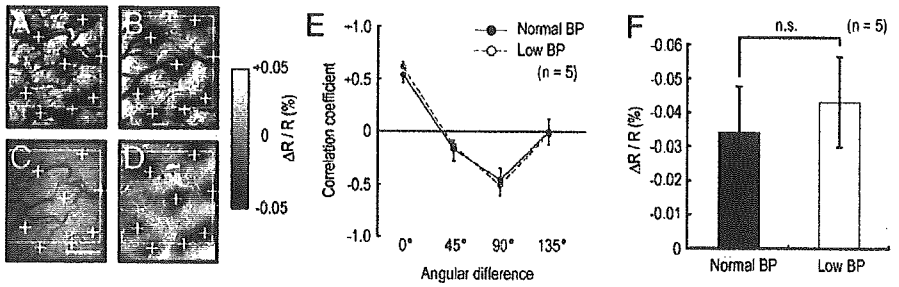

Fig. 6. Preservation of orientation selectivity of dHb signals during low BP. (A and B) Single-condition iso-orientation maps at 620 nm for visual stimulation with a grating orientation of 45° during normal (A) and low (B) BP. Data for the maps were obtained from the *Single-orientation 620-nm OIS* experiment and averaged from 0.5 to 10 s after stimulus onset (during stimulation). The data are from the same study as Figs. 5A and B. Note that global reflection changes were filtered out (see Figs. 1B–E). (C) A cortical surface image at 540 nm shows pial vessels for reference to the maps in panels A, B, and D. The scale bar is 1 mm. (D) Differential iso-orientation map at 620 nm obtained from the *Four-orientation 620-nm OIS* experiment. Black patches in panels A, B, and D are selective responses to the grating at 45° orientation. Locations of the patches were determined on the differential map and marked with white crosses on all images. The white rectangles are the regions (100 × 100 pixels) for calculating correlation coefficient in this example. (E) Average correlation coefficients (n = 5 cats) based comparisons on a pixel to pixel basis. The horizontal axis represents the angular difference of stimulus orientations between the single-condition and the differential iso-orientation data, where single-condition iso-orientation maps were obtained at only one orientation during both normal (filled circles) and low (open circles) BP, and differential iso-orientation maps were obtained at normal BP for four different orientations. 0° indicates that the single-condition vs. differential map comparisons are for identical stimuli, while 90° indicates that the comparisons are for orthogonal orientations. Error bars are ±1 SD (only one side is plotted). (F) Average magnitude difference (i.e., 'active domain' minus 'inactive domain'). Error bars are ±1 SD. The n.s. indicates that there was no statistically significant difference (P = 0.25, n = 5 cats).